

CERN-PH-EP-2014-091
13 May 2014

3 **Neutral pion production at midrapidity in pp and Pb-Pb collisions at**
4 **$\sqrt{s_{NN}} = 2.76$ TeV**

5 ALICE Collaboration*

6 **Abstract**

7 Invariant yields of neutral pions at midrapidity in the transverse momentum range $0.6 < p_T <$
8 12 GeV/ c measured in Pb-Pb collisions at $\sqrt{s_{NN}} = 2.76$ TeV are presented for six centrality classes.
9 The pp reference spectrum was measured in the range $0.4 < p_T < 10$ GeV/ c at the same center-of-
10 mass energy. The nuclear modification factor, R_{AA} , shows a suppression of neutral pions in central
11 Pb-Pb collisions by a factor of up to about 8 – 10 for $5 \lesssim p_T \lesssim 7$ GeV/ c . The presented measurements
12 are compared with results at lower center-of-mass energies and with theoretical calculations.

*See Appendix A for the list of collaboration members

1 Introduction

Quantum chromodynamics (QCD) predicts a transition from hadronic matter to a state of deconfined quarks and gluons, i.e., to the quark-gluon plasma (QGP), at a temperature of $T_c \approx 150 - 160$ MeV at vanishing net baryon number [1,2]. Energy densities created in Pb-Pb collisions at the LHC are estimated to be sufficiently large to reach this state [3,4]. At low transverse momenta (roughly $p_T \lesssim 3$ GeV/c) it is expected that pressure gradients in the QGP produced in an ultrarelativistic collision of two nuclei give rise to a collective, outward-directed velocity profile, resulting in a characteristic modification of hadron spectra [5]. At sufficiently large p_T ($\gtrsim 3 - 8$ GeV/c), hadrons in pp and Pb-Pb collisions originate from hard scattering as products of jet fragmentation. Hard-scattered quarks and gluons, produced in the initial stage of the heavy-ion collision, must traverse the QGP that is produced around them and lose energy in the process through interactions with that medium. This phenomenon (“jet quenching”) leads to a modification of hadron yields at high p_T [6, 7]. By studying observables related to jet quenching one would like to better understand the mechanism of parton energy loss and to use hard probes as a tool to characterize the QGP.

The modification of the hadron yields for different p_T intervals in heavy-ion (A-A) collisions with respect to pp collisions can be quantified with the nuclear modification factor

$$R_{AA}(p_T) = \frac{d^2N/dp_T dy|_{AA}}{\langle T_{AA} \rangle \times d^2\sigma/dp_T dy|_{pp}} \quad (1)$$

where the nuclear overlap function $\langle T_{AA} \rangle$ is related to the average number of inelastic nucleon-nucleon collisions as $\langle T_{AA} \rangle = \langle N_{\text{coll}} \rangle / \sigma_{\text{inel}}^{\text{pp}}$. In the factorization approach of a perturbative QCD calculation of particle production from hard scattering, the overlap function T_{AA} can be interpreted as the increase of the parton flux in going from pp to A-A collisions. Without nuclear effects, R_{AA} will be unity in the hard scattering regime.

Parton energy loss depends on a number of factors including the transport properties of the medium and their space-time evolution, the initial parton energy, and the parton type [8–12]. The nuclear modification factor, R_{AA} , is also affected by the slope of the initial parton transverse momentum spectrum prior to any interaction with the medium and initial-state effects like the modifications of the parton distributions in nuclei. An important constraint for modeling these effects comes from the study of p-A collisions [13], but also from the study of A-A collisions at different center-of-mass energies ($\sqrt{s_{\text{NN}}}$) and different centralities. For instance, the increase in $\sqrt{s_{\text{NN}}}$ from RHIC to LHC energies by about a factor 14 results in larger initial energy densities and less steeply falling initial parton spectra [14]. Moreover, at the LHC, pions with $p_T \lesssim 50$ GeV/c are dominantly produced in the fragmentation of gluons [15], whereas the contribution from quark fragmentation in the same p_T region is much larger and more strongly varying with p_T at RHIC [16]. Therefore, the pion suppression results at the LHC will be dominated by gluon energy loss, and simpler to interpret than the results from RHIC. Compared to measurements of the R_{AA} for inclusive charged hadrons, differences between the baryon and meson R_{AA} provide additional information on the parton energy loss mechanism and/or on hadronization in A-A collisions [17, 18]. Experimentally, neutral pions are ideally suited for this as they can be cleanly identified (on a statistical basis) via the decay $\pi^0 \rightarrow \gamma\gamma$.

The suppression of neutral pions and charged hadrons at large transverse momentum [19–23] and the disappearance of azimuthal back-to-back correlations of charged hadrons in central Au-Au collision at RHIC [24, 25] (see also [26–29]) were interpreted in terms of parton energy loss in hot QCD matter. Neutral pions in central Au-Au collisions at $\sqrt{s_{\text{NN}}} = 200$ GeV were found to be suppressed by a factor of 4–5 for $p_T \gtrsim 4$ GeV/c [30, 31]. The rather weak dependence of R_{AA} on p_T was described by a large number of jet quenching models [32]. The $\sqrt{s_{\text{NN}}}$ and system size dependence was studied in Cu-Cu collisions at $\sqrt{s_{\text{NN}}} = 19.4, 62.4,$ and 200 GeV [33] and in Au-Au collisions at $\sqrt{s_{\text{NN}}} = 39, 62.4,$ and 200 GeV [22, 34]. In central Cu-Cu collisions the onset of $R_{AA} < 1$ was found to occur between

58 $\sqrt{s_{\text{NN}}} = 19.4$ and 62.4 GeV. For unidentified charged hadrons in central Pb-Pb collisions at the LHC,
 59 R_{AA} was found to increase from $R_{\text{AA}} < 0.2$ at $p_{\text{T}} \approx 7$ GeV/ c to $R_{\text{AA}} \approx 0.5$ for $p_{\text{T}} \gtrsim 50$ GeV/ c , in line
 60 with a decrease of the relative energy loss with increasing parton p_{T} [35–37].

61 The dependence of the neutral pion R_{AA} on $\sqrt{s_{\text{NN}}}$ and p_{T} in Au-Au collisions at RHIC energies for
 62 $2 \lesssim p_{\text{T}} \lesssim 7$ GeV/ c is not fully reproduced by jet quenching calculations in the GLV framework which is
 63 based on perturbative QCD [34, 38, 39]. This may indicate that, especially for this intermediate p_{T} range,
 64 jet quenching calculations do not yet fully capture the relevant physics processes. With the large increase
 65 in $\sqrt{s_{\text{NN}}}$ the measurement of R_{AA} at the LHC provides a large lever arm to further constrain parton
 66 energy loss models. Phenomena affecting pion production in the p_{T} range $0.6 < p_{\text{T}} < 12$ GeV/ c of this
 67 measurement include collective radial flow at low p_{T} and parton energy loss at high p_{T} . The data are
 68 therefore well suited to test models aiming at a description of particle production over the full transverse
 69 momentum range, including the potentially complicated interplay between jets and the evolving medium.

70 2 Detector description

71 Neutral pions were reconstructed via the two-photon decay channel $\pi^0 \rightarrow \gamma\gamma$ which has a branching ratio
 72 of 98.8% [40]. Two independent methods of photon detection were employed: with the Photon Spec-
 73 trometer (PHOS) which is an electromagnetic calorimeter [41], and with photon conversions measured
 74 in the central tracking system using the Inner Tracking System (ITS) [42] and the Time Projection Cham-
 75 ber (TPC) [43]. In the latter method, referred to as Photon Conversion Method (PCM), conversions out
 76 to the middle of the TPC were reconstructed (radial distance $R \approx 180$ cm). The material in this range
 77 amounts to $(11.4 \pm 0.5)\%$ of a radiation length X_0 for $|\eta| < 0.9$ corresponding to a plateau value of the
 78 photon conversion probability of $(8.6 \pm 0.4)\%$. The measurement of neutral pions with two independent
 79 methods with different systematics and with momentum resolutions having opposite dependence on mo-
 80 mentum provides a valuable check of the systematic uncertainties and facilitates the measurements of
 81 neutral pions in a wide momentum range with small systematic uncertainty.

82 PHOS consists of three modules installed at a distance of 4.6 m from the interaction point. PHOS
 83 subtends $260^\circ < \varphi < 320^\circ$ in azimuth and $|\eta| < 0.13$ in pseudorapidity. Each module has 3584 detection
 84 channels in a matrix of 64×56 cells made of lead tungstate (PbWO_4) crystals each of size $2.2 \times 2.2 \times$
 85 18 cm³. The transverse dimensions of the cells are slightly larger than the PbWO_4 Molière radius of
 86 2 cm. The signals from the cells are measured by avalanche photodiodes with a low-noise charge-
 87 sensitive preamplifier. In order to increase the light yield and thus to improve energy resolution, PHOS
 88 crystals are cooled down to a temperature of -25 °C. The PHOS cells were calibrated in pp collisions
 89 by equalizing the π^0 peak position for all cell combinations registering a hit by a decay photon.

90 The Inner Tracking System (ITS) [44] consists of two layers of Silicon Pixel Detectors (SPD) positioned
 91 at a radial distance of 3.9 cm and 7.6 cm, two layers of Silicon Drift Detectors (SDD) at 15.0 cm and
 92 23.9 cm, and two layers of Silicon Strip Detectors (SSD) at 38.0 cm and 43.0 cm. The two SPD layers
 93 cover a pseudorapidity range of $|\eta| < 2$ and $|\eta| < 1.4$, respectively. The SDD and the SSD subtend
 94 $|\eta| < 0.9$ and $|\eta| < 1.0$, respectively.

95 The Time Projection Chamber (TPC) [43] is a large (85 m³) cylindrical drift detector filled with a
 96 Ne/CO₂/N₂ (85.7/9.5/4.8%) gas mixture. It covers a pseudorapidity range of $|\eta| < 0.9$ over the full
 97 azimuthal angle for the maximum track length of 159 reconstructed space points. With the magnetic
 98 field of $B = 0.5$ T, electron and positron tracks were reconstructed down to transverse momenta of about
 99 50 MeV/ c . In addition, the TPC provides particle identification via the measurement of the specific en-
 100 ergy loss (dE/dx) with a resolution of 5.5% [43]. The ITS and the TPC were aligned with respect to each
 101 other to a precision better than 100 μm using tracks from cosmic rays and proton-proton collisions [42].

102 Two forward scintillator hodoscopes (VZERO-A and VZERO-C) [45] subtending $2.8 < \eta < 5.1$ and

103 $-3.7 < \eta < -1.7$, respectively, were used in the minimum bias trigger in the pp and in the Pb-Pb
 104 run. The sum of the amplitudes of VZERO-A and VZERO-C served as a measure of centrality in Pb-
 105 Pb collisions [46]. Spectator (non-interacting) protons and neutrons were measured with Zero Degree
 106 Calorimeters (ZDCs), located close to the beam pipe, 114 m away from the interaction point on either
 107 side of the ALICE detector [44].

108 3 Data processing

109 3.1 Event selection

110 The pp sample at $\sqrt{s} = 2.76$ TeV was collected in the 2011 LHC run. The minimum bias trigger (MB_{OR})
 111 in the pp run required a hit in either VZERO hodoscope or a hit in the SPD. Based on a van der Meer
 112 scan the cross section for inelastic pp collisions was determined to be $\sigma_{\text{inel}} = (62.8_{-4.0}^{+2.4} \pm 1.2)$ mb and
 113 the MB_{OR} trigger had an efficiency of $\sigma_{\text{MBOR}}/\sigma_{\text{inel}} = 0.881_{-0.035}^{+0.059}$ [47]. The results were obtained from
 114 samples of 34.7×10^6 (PHOS) and 58×10^6 (PCM) minimum bias pp collisions corresponding to an in-
 115 tegrated luminosity $\mathcal{L}_{\text{int}} = 0.63 \text{ nb}^{-1}$ and $\mathcal{L}_{\text{int}} = 1.05 \text{ nb}^{-1}$, respectively. PHOS and the central tracking
 116 detectors used in the PCM were in different readout partitions of the ALICE experiment which resulted
 117 in the different integrated luminosities.

118 The Pb-Pb data at $\sqrt{s_{\text{NN}}} = 2.76$ TeV were recorded in the 2010 LHC run. At the ALICE interaction
 119 region up to 114 bunches, each containing about 7×10^7 ²⁰⁸Pb ions, were collided. The rate of hadronic
 120 interactions was about 100 Hz, corresponding to a luminosity of about $1.3 \times 10^{25} \text{ cm}^{-2}\text{s}^{-1}$. The detector
 121 readout was triggered by the LHC bunch-crossing signal and a minimum bias interaction trigger based
 122 on trigger signals from VZERO-A, VZERO-C, and SPD [46]. The efficiency for triggering on a hadronic
 123 Pb-Pb collision ranged between 98.4% and 99.7%, depending on the minimum bias trigger configuration.
 124 For the centrality range 0-80% studied in the Pb-Pb analyses 16.1×10^6 events in the PHOS analysis and
 125 13.2×10^6 events in the PCM analysis passed the offline event selection.

126 In both pp and Pb-Pb analyses, the event selection was based on VZERO timing information and on the
 127 correlation between TPC tracks and hits in the SPD to reject background events coming from parasitic
 128 beam interactions. In addition, an energy deposit in the ZDCs of at least three standard deviations
 129 above the single-neutron peak was required for Pb-Pb collisions to further suppress electromagnetic
 130 interactions [46]. Only events with a reconstructed vertex in $|z_{\text{vtx}}| < 10$ cm with respect to the nominal
 131 interaction vertex position along the beam direction were used.

132 3.2 Neutral pion reconstruction

133 The PHOS and PCM analyses presented here are based on methods previously used in pp collisions at
 134 $\sqrt{s} = 0.9$ and 7 TeV [48]. Neutral pions were reconstructed using the $\pi^0 \rightarrow \gamma\gamma$ decay channel either with
 135 both photon candidates detected in PHOS or both photons converted into e^+e^- pairs and reconstructed in
 136 the central tracking system. For the photon measurement with PHOS adjacent lead tungstate cells with
 137 energy signals above a threshold (12 MeV) were grouped into clusters [49]. The energies of the cells
 138 in a cluster were summed up to determine the photon energy. The selection of the photon candidates
 139 in PHOS was different for pp and Pb-Pb collisions due to the large difference in detector occupancy.
 140 For pp collisions cluster overlap is negligible and combinatorial background small. Therefore, only
 141 relatively loose photon identification cuts on the cluster parameters were used in order to maximize the
 142 π^0 reconstruction efficiency: the cluster energy for pp collisions was required to be above the minimum
 143 ionizing energy $E_{\text{cluster}} > 0.3$ GeV and the number of cells in a cluster was required to be greater than
 144 two to reduce the contribution of hadronic clusters. In the case of the most central Pb-Pb collisions
 145 about 80 clusters are reconstructed in PHOS, resulting in an occupancy of up to 1/5 of the 10752 PHOS
 146 cells. This leads to a sizable probability of cluster overlap and to a high combinatorial background in the
 147 two-cluster invariant mass spectra. A local cluster maximum was defined as a cell with a signal at least

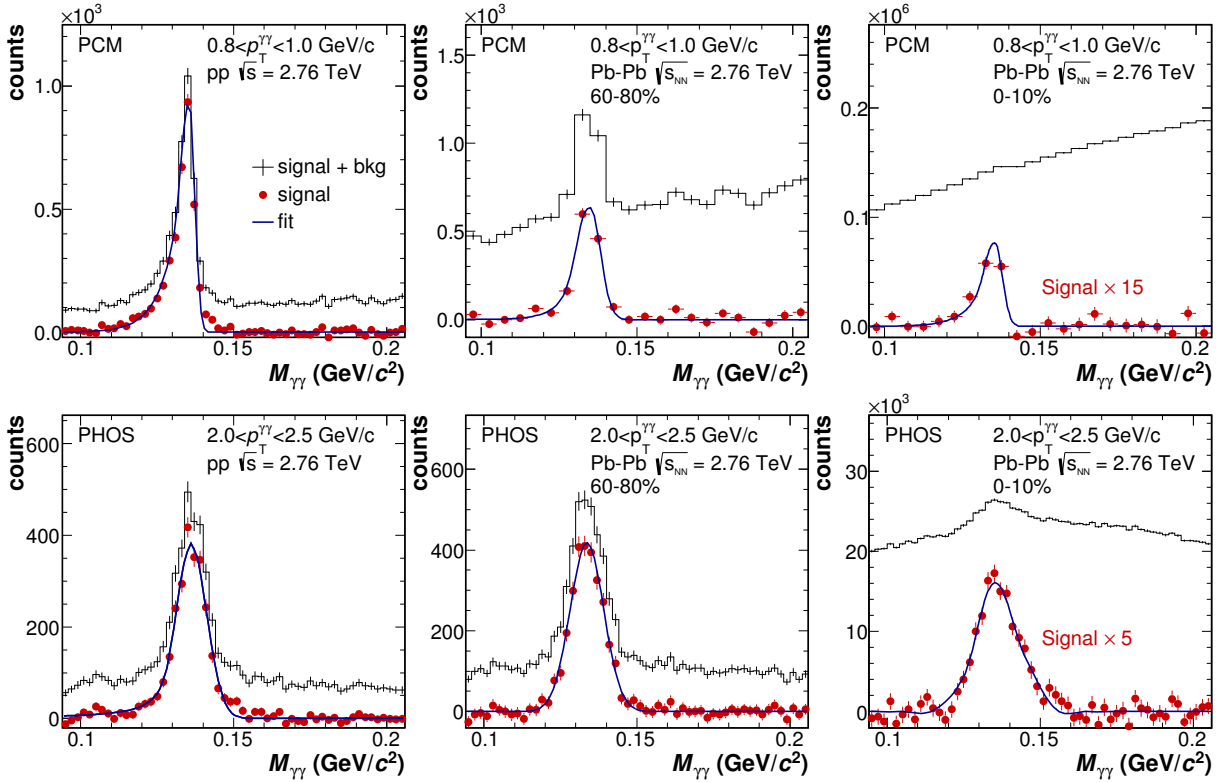


Fig. 1: (Color online) Invariant mass spectra in selected p_T slices for PCM (upper row) and PHOS (lower row) in the π^0 mass region for pp (left column), 60 – 80% (middle column) and 0 – 10% (right column) Pb-Pb collisions. The histogram and the filled points show the data before and after background subtraction, respectively. For the 0 – 10% class the invariant mass distributions after background subtraction were scaled by a factor 15 and 5 for PCM and PHOS, respectively, for better visibility of the peak. The positions and widths of the π^0 peaks were determined from the fits, shown as blue curves, to the invariant mass spectra after background subtraction.

148 30 MeV higher than the signal in each surrounding cell. A cluster with more than one local maximum
 149 was unfolded to several contributing clusters. As the lateral width of showers resulting from hadrons is
 150 typically larger than the one of photon showers, non-photon background was reduced by a p_T dependent
 151 shower shape cut. This cut is based on the eigenvalues λ_0, λ_1 of the covariance matrix built from the cell
 152 coordinates and weights $w_i = \max[0, w_0 + \log(E_i/E_{\text{cluster}})]$, $w_0 = 4.5$ where E_i is the energy measured in
 153 cell i . In the Pb-Pb case only cells with a distance to the cluster center of $R_{\text{disp}} = 4.5$ cm were used in
 154 the dispersion calculation. A 2D p_T -dependent cut in the λ_0 - λ_1 plane was tuned to have an efficiency of
 155 ~ 0.95 using pp data. In addition, clusters associated with a charged particle were rejected by application
 156 of a cut on the minimum distance from a PHOS cluster to the extrapolation of reconstructed tracks to
 157 the PHOS surface [49]. This distance cut depended on track momentum and was tuned by using real
 158 data to minimize false rejection of photon clusters resulting. The corresponding loss of the π^0 yield was
 159 about 1% in pp collisions. In Pb-Pb collisions the π^0 inefficiency due to the charged particle rejection
 160 is about 1% in peripheral and increases to about 7% in central Pb-Pb collisions. In addition, to reduce
 161 the effect of cluster overlap, the cluster energy was taken as the *core energy* of the cluster, summing over
 162 cells with centers within a radius $R_{\text{core}} = 3.5$ cm of the cluster center of gravity, rather than summing
 163 over all cells of the cluster. By using the core energy, the centrality dependence of the width and position
 164 of the π^0 peak is reduced, due to a reduction of overlap effects. The use of the core energy leads to an
 165 additional non-linearity due to energy leakage outside R_{core} : the difference between full and core energy
 166 is negligible at $E_{\text{cluster}} \lesssim 1$ GeV and reaches $\sim 4\%$ at $E_{\text{cluster}} \sim 10$ GeV. This non-linearity, however, is
 167 well reproduced in the GEANT3 Monte Carlo simulations [50] of the PHOS detector response (compare
 168 p_T dependences of peak positions in data and MC in Fig. 2) and is corrected for in the final spectra.

169 PHOS is sensitive to pile-up from multiple events that occur within the 6 μs readout interval of the PHOS
 170 front-end electronics. The shortest time interval between two bunch crossings in pp collisions was 525 ns.
 171 To suppress photons produced in other bunch crossings, a cut on arrival time $|t| < 265$ ns was applied
 172 to reconstructed clusters which removed 16% of the clusters. In the Pb-Pb collisions, the shortest time
 173 interval between bunch crossing was 500 ns, but the interaction probability per bunch crossing was much
 174 smaller than in pp collisions. To check for a contribution from other bunch crossings to the measured
 175 spectra, a timing cut was applied, and the pile-up contribution was found to be negligible in all centrality
 176 classes. Therefore, a timing cut was not applied in the final PHOS Pb-Pb analysis.

177 The starting point of the conversion analysis is a sample of photon candidates corresponding to track
 178 pairs reconstructed by a secondary vertex (V0) finding algorithm [49, 51]. In this step, no constraints
 179 on the reconstructed invariant mass and pointing of the momentum vector to the collision vertex were
 180 applied. Both tracks of a V0 were required to contain reconstructed clusters (i.e., space points) in the
 181 TPC. V0's were accepted as photon candidates if the ratio of the number of reconstructed TPC clusters
 182 over the number of findable clusters (taking into account track length, spatial location, and momentum)
 183 was larger than 0.6 for both tracks. In order to reject K_S^0 , Λ , and $\bar{\Lambda}$ decays, electron selection and pion
 184 rejection cuts were applied. V0's used as photon candidates were required to have tracks with a specific
 185 energy loss in the TPC within a band of $[-3\sigma, 5\sigma]$ around the average electron dE/dx , and of more
 186 than 3σ above the average pion dE/dx (where the second condition was only applied for tracks with
 187 measured momenta $p > 0.4$ GeV/ c). Moreover, tracks with an associated signal in the TOF detector
 188 were only accepted as photon candidates if they were consistent with the electron hypothesis within
 189 a $\pm 5\sigma$ band. A generic particle decay model based on the Kalman filter method [52] was fitted to a
 190 reconstructed V0 assuming that the particle originated from the primary vertex and had a mass $M_{V0} = 0$.
 191 Remaining contamination in the photon sample was reduced by cutting on the χ^2 of this fit. Furthermore,
 192 the transverse momentum $q_T = p_e \sin \theta_{V0,e}$ [53] of the electron, p_e , with respect to the V0 momentum
 193 was restricted to $q_T < 0.05$ GeV/ c . As the photon is massless, the difference $\Delta\theta = |\theta_{e^-} - \theta_{e^+}|$ of the
 194 polar angles of the electron and the positron from a photon conversion is small and the bending of the
 195 tracks in the magnetic field only results in a difference $\Delta\phi = |\phi_{e^-} - \phi_{e^+}|$ of the azimuthal angles of the
 196 two momentum vectors. Therefore, remaining random track combinations, reconstructed as a V0, were
 197 suppressed further by a cut on the ratio of $\Delta\theta$ to the total opening angle of the e^+e^- pair calculated after
 198 propagating both the electron and the positron 50 cm from the conversion point in the radial direction.
 199 In order to reject e^+e^- pairs from Dalitz decays the distance between the nominal interaction point and
 200 the reconstructed conversion point of a photon candidate had to be larger than 5 cm in radial direction.
 201 The maximum allowed radial distance for reconstructed V0's was 180 cm.

202 Pile-up of neutral pions coming from bunch crossings other than the triggered one also has an effect on
 203 the PCM measurement. At the level of reconstructed photons, this background is largest for photons for
 204 which both the electron and the positron were reconstructed with the TPC alone without tracking infor-
 205 mation from the ITS. These photons, which typically converted at large radii R , constitute a significant
 206 fraction of the total PCM photon sample, which is about 67% in case of the pp analysis. This sample is
 207 affected because the TPC drift velocity of 2.7 cm/ μs corresponds to a drift distance of 1.41 cm between
 208 two bunch crossings in the pp run which is a relatively short distance compared to the width of $\sigma_z \approx 5$ cm
 209 of the distribution of the primary vertex in the z direction. The distribution of the distance of closest ap-
 210 proach in the z direction (DCA_z) of the straight line defined by the reconstructed photon momentum is
 211 wider for photons from bunch crossings other than the triggered one. The DCA_z distribution of photons
 212 which had an invariant mass in the π^0 mass range along with a second photon was measured for each
 213 p_T interval. Entries in the tails at large DCA_z were used to determine the background distribution and to
 214 correct the neutral pion yields for inter bunch pile-up. For the pp analysis, this was a 5 – 7% correction
 215 for $p_T \gtrsim 2$ GeV/ c and a correction of up to 15% at lower p_T ($p_T \approx 1$ GeV/ c). In the Pb-Pb case the
 216 correction at low p_T was about 10%, and became smaller for higher p_T and for more central collisions.
 217 For the 20 – 40% centrality class and more central classes the pile-up contribution was negligible and

no pile-up correction was applied. In the PCM as well as in the PHOS analysis, events for which two or more pp or Pb-Pb interactions occurred in the same bunch crossing were rejected based on the number of primary vertices reconstructed with the SPD [49] which has an integration time of less than 200 ns.

In the PHOS as well as in the PCM analysis, the neutral pion yield was extracted from a peak above a combinatorial background in the two-photon invariant mass spectrum. Examples of invariant mass spectra, in the π^0 mass region, are shown in Fig. 1 for selected p_T bins for pp collisions, and peripheral and central Pb-Pb collisions. The combinatorial background was determined by mixing photon candidates from different events of the same centrality class and with similar z vertex positions. Mixed events in Pb-Pb collisions were constructed by taking events from the same centrality class. In the PCM measurement the combinatorial background was reduced by cutting on the energy asymmetry $\alpha = |E_{\gamma_1} - E_{\gamma_2}| / (E_{\gamma_1} + E_{\gamma_2})$, where $\alpha < 0.65$ was required for the central classes (0 – 5%, 5 – 10%, 10 – 20%, 20 – 40%) and $\alpha < 0.8$ for the two peripheral classes (40 – 60%, 60 – 80%). In both analyses the mixed-event background distributions were normalized to the right and left sides of the π^0 peak. A residual correlated background was taken into account using a linear or second order polynomial fit. The π^0 peak parameters were obtained by fitting a function, Gaussian or a Crystal Ball function [54] in the PHOS case or asymmetric Gaussian [55] in the PCM case, to the background-subtracted invariant mass distribution, see Fig. 1. In the case of PHOS the number of reconstructed π^0 's was obtained in each p_T bin by integrating the background subtracted peak within 3 standard deviations around the mean value of the π^0 peak position. In the PCM analysis, the integration window was chosen to be asymmetric ($m_{\pi^0} - 0.035 \text{ GeV}/c^2$, $m_{\pi^0} + 0.010 \text{ GeV}/c^2$) to take into account the left side tail of the π^0 peak due to bremsstrahlung energy loss of electrons and positrons from photon conversions. In both analyses the normalization and integration windows were varied to estimate the related systematic uncertainties. The peak positions and widths from the two analyses are compared to GEANT3 Monte Carlo simulations in Fig. 2 as a function of p_T . The input for the GEANT3 simulation came from the event generators PYTHIA 8 [56] and PHOJET [57] in the case of pp collisions (with roughly equal number of events) and from HIJING [58] in the case of Pb-Pb collisions. For the PCM analysis the full width at half maximum (FWHM) divided by 2.35 is shown. Note the decrease of the measured peak position with p_T in Pb-Pb collisions for PHOS. This is due to the use of the core energy instead of the full cluster energy. At low p_T in central Pb-Pb collisions, shower overlaps can increase the cluster energy thereby resulting in peak positions above the nominal π^0 mass. A good agreement in peak position and width between data and simulation is observed in both analyses. The remaining small deviations in the case of PHOS were taken into account as a systematic uncertainty related to the global energy scale.

The correction factor $\varepsilon(p_T)$ for the PHOS detector response and the acceptance $A(p_T)$ were calculated with GEANT3 Monte Carlo simulations tuned to reproduce the detector response. In the case of Pb-Pb collisions the embedding technique was used in the PHOS analysis: the PHOS response to single π^0 's was simulated, the simulated π^0 event was added to a real Pb-Pb event on the cell signal level, after which the standard reconstruction procedure was performed. The correction factor $\varepsilon(p_T) = (N_{\text{rec}}^{\text{after}}(p_T) - N_{\text{rec}}^{\text{before}}(p_T)) / N_{\text{sim}}(p_T)$ was defined as the ratio of the difference of the number of reconstructed π^0 's after and before the embedding to the number of simulated π^0 's. In the pp case, the PHOS occupancy was so low that embedding was not needed and $\varepsilon(p_T)$ was obtained from the π^0 simulations alone. Both in the Pb-Pb and the pp analysis, an additional 2% channel-by-channel decalibration was introduced to the Monte Carlo simulations, as well as an energy non-linearity observed in real data at low energies which is not reproduced by the GEANT simulations. This non-linearity is equal to 2.2% at $p_T = 1 \text{ GeV}/c$ and decreases rapidly with p_T (less than 0.5% at $p_T > 3 \text{ GeV}/c$). For PHOS, the π^0 acceptance A is zero for $p_T < 0.4 \text{ GeV}/c$. The product $\varepsilon \cdot A$ increases with p_T and saturates at about 1.4×10^{-2} for a neutral pion with $p_T > 15 \text{ GeV}/c$. At high transverse momenta ($p_T > 25 \text{ GeV}/c$) ε decreases due to merging of clusters of π^0 decay photons due to decreasing of average opening angle. The correction factor ε does not show a centrality dependence for events in the 20 – 80% class, but in the most central bin it increases by $\sim 10\%$ due to an increase in cluster energies caused by cluster overlap.

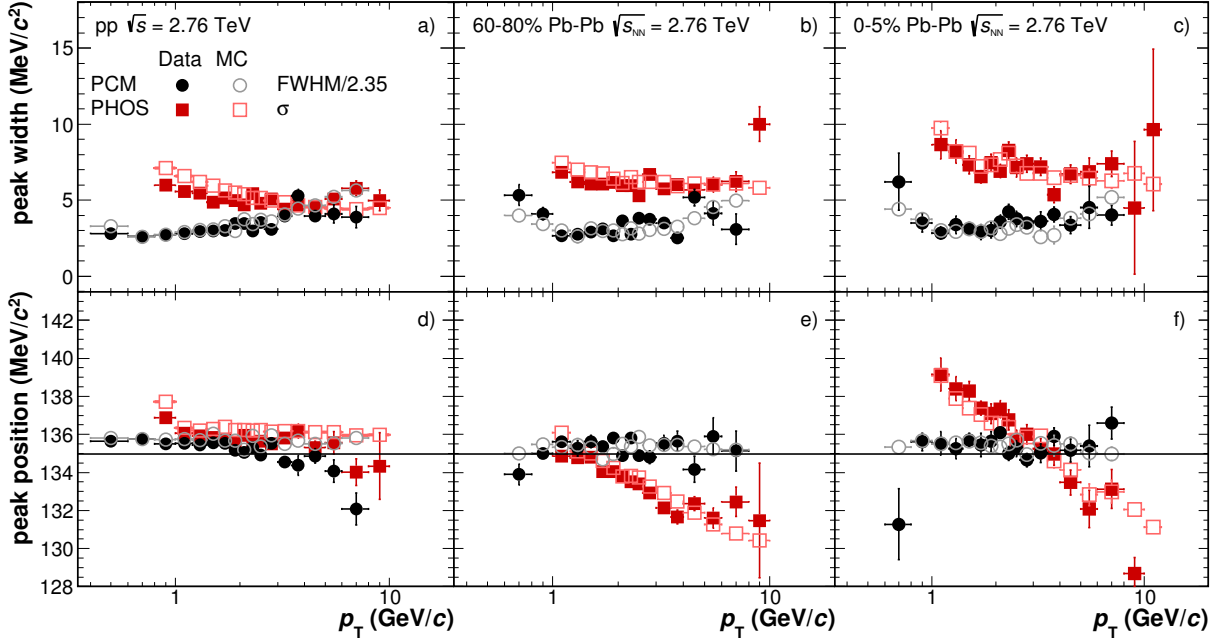


Fig. 2: (Color online) Reconstructed π^0 peak width (upper row) and position (lower row) as a function of p_T in pp collisions at $\sqrt{s} = 2.76$ TeV (a, d), peripheral (b, e) and central (c, f) Pb-Pb collisions at $\sqrt{s_{NN}} = 2.76$ TeV in PHOS and in the photon conversion method (PCM) compared to Monte Carlo simulations. The horizontal line in (d, e, f) indicates the nominal π^0 mass.

267 In the PCM, the photon conversion probability of about 8.6% is compensated by the large TPC accep-
 268 tance. Neutral pions were reconstructed in the rapidity interval $|y| < 0.6$ and the decay photons were
 269 required to satisfy $|\eta| < 0.65$. The π^0 efficiency increases with p_T below $p_T \approx 4$ GeV/c and remains
 270 approximately constant for higher p_T at values between 1.0×10^{-3} in central collisions (0 – 5%, energy
 271 asymmetry cut $\alpha < 0.65$) and 1.5×10^{-3} in peripheral collisions (60 – 80%, $\alpha < 0.8$). For the centrality
 272 classes 0 – 5%, 5 – 10%, 10 – 20%, 20 – 40%, for which $\alpha < 0.65$ was used, the π^0 efficiency varies
 273 between 1.0×10^{-3} and 1.2×10^{-3} . This small centrality dependence is dominated by the centrality de-
 274 pendence of the V0 finding efficiency. Further information on the PHOS and PCM efficiency corrections
 275 can be found in [49].

276 The invariant differential neutral pion yield was calculated as

$$E \frac{d^3N}{d^3p} = \frac{1}{2\pi} \frac{1}{N_{\text{events}}} \frac{1}{p_T} \frac{1}{\epsilon A} \frac{1}{Br} \frac{1}{\Delta y \Delta p_T} N^{\pi^0}, \quad (2)$$

277 where N_{events} is the number of events; p_T is the transverse momentum within the bin to which the cross
 278 section has been assigned after the correction for the finite bin width Δp_T , Br is the branching ratio of
 279 the decay $\pi^0 \rightarrow \gamma\gamma$, and N^{π^0} is the number of reconstructed π^0 's in a given Δy and Δp_T bin. Finally,
 280 the invariant yields were corrected for the finite p_T bin width following the prescription in [59], i.e., by
 281 plotting the measured average yield at a p_T position for which the differential invariant yield coincides
 282 with the bin average. Secondary π^0 's from weak decays or hadronic interactions in the detector material
 283 were subtracted using Monte Carlo simulations. The contribution of π^0 's from K_s^0 as obtained from the
 284 used event generators was scaled in order to reproduce the measured K_s^0 yields [60]. The correction for
 285 secondary π^0 's was smaller than 2% (5%) for $p_T \gtrsim 2$ GeV/c in the pp as well as in the Pb-Pb analysis
 286 for PCM (PHOS).

287 A summary of the systematic uncertainties for two representative p_T values in pp, peripheral and central
 288 Pb-Pb collisions is shown in Table 1. In PHOS, one of the largest sources of the systematic uncertainty
 289 both at low and high p_T is the raw yield extraction. It was estimated by varying the fitting range and

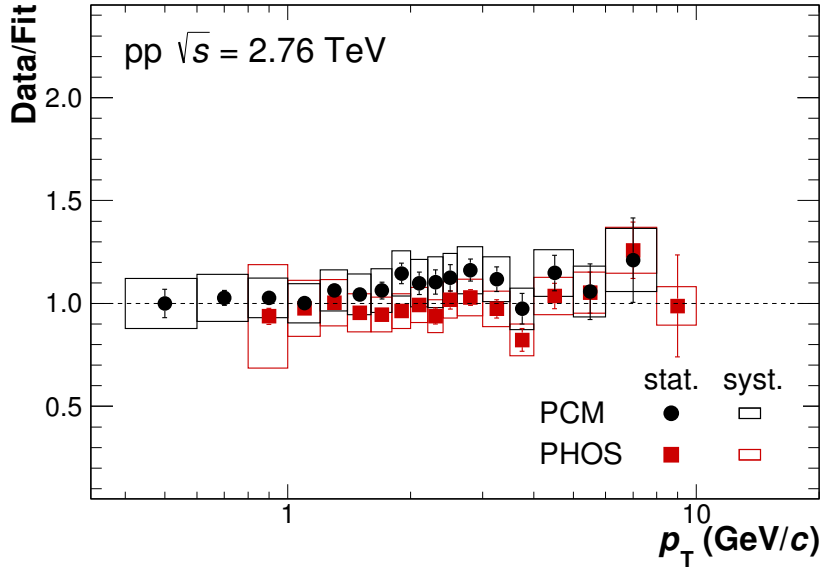


Fig. 3: (Color online) Ratio of the fully corrected π^0 spectra in pp collisions at $\sqrt{s} = 2.76$ TeV measured with PHOS and PCM methods to the fit of the combined spectrum. Vertical lines represent statistical uncertainties, the boxes systematic uncertainties.

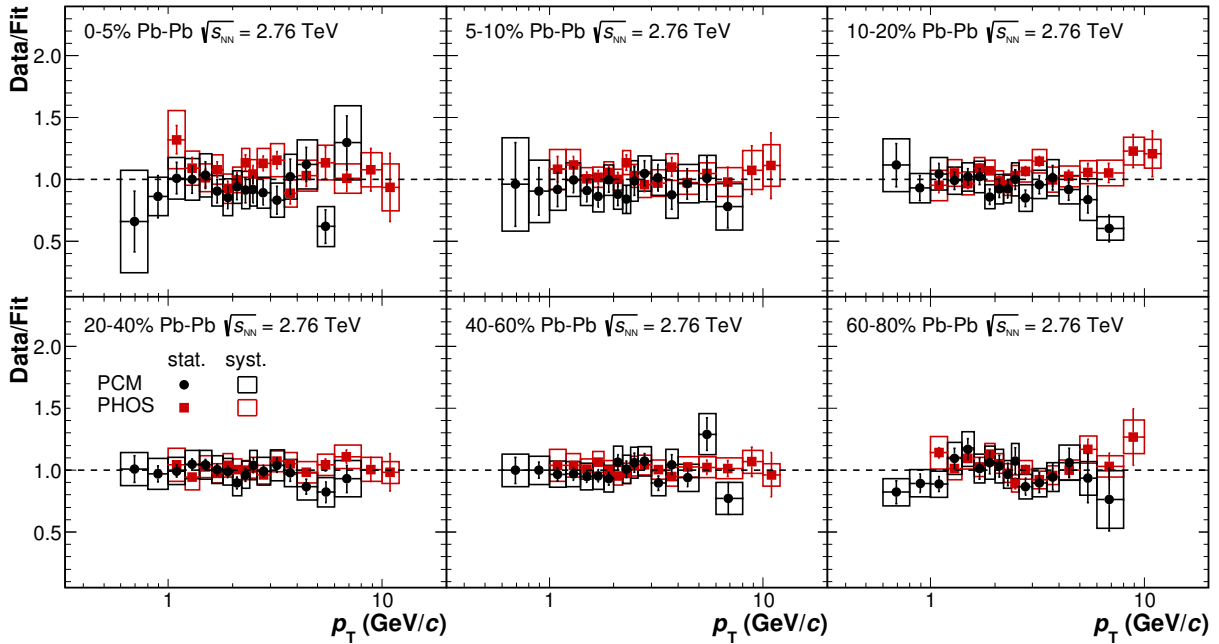


Fig. 4: (Color online) Ratio of the fully corrected π^0 spectra in Pb-Pb collisions at $\sqrt{s_{NN}} = 2.76$ TeV in six centrality bins measured with PHOS and PCM to the fits to the combined result in each bin. Vertical lines represent statistical uncertainties, the boxes the systematic uncertainties.

290 the assumption about the shape of the background under the peak. In central collisions, major contribu-
 291 tions to the systematic uncertainty are due to the efficiency of photon identification and the global energy
 292 scale. The former was evaluated by comparing efficiency-corrected π^0 yields, calculated with different
 293 identification criteria. The latter was estimated by varying the global energy scale within the tolerance
 294 which would still allow to reproduce the peak position in central and peripheral collisions. The uncer-
 295 tainty related to the non-linearity of the PHOS energy response was estimated by introducing different
 296 non-linearities into the MC simulations under the condition that the simulated p_T dependence of the π^0

Table 1: Summary of the relative systematic uncertainties in percent for selected p_T bins for the PHOS and the PCM analyses.

	PHOS					
	pp		Pb-Pb, 60 – 80%		Pb-Pb, 0 – 5%	
	1.1 GeV/c	7.5 GeV/c	3 GeV/c	10 GeV/c	3 GeV/c	10 GeV/c
Yield extraction	8	2.3	0.8	6.8	3.7	5.7
Photon identification	–	–	1.7	1.7	4.4	4.4
Global E scale	4	6.2	4.1	5.3	6.1	7.8
Non-linearity	9	1.5	1.5	1.5	1.5	1.5
Conversion	3.5	3.5	3.5	3.5	3.5	3.5
Module alignment	4.1	4.1	4.1	4.1	4.1	4.1
Other	2	1.4	2.4	2.4	3.1	3.4
Total	13.9	8.8	7.6	10.7	10.7	12.7
	PCM					
	pp		Pb-Pb, 60 – 80%		Pb-Pb, 0 – 5%	
	1.1 GeV/c	5.0 GeV/c	1.1 GeV/c	5.0 GeV/c	1.1 GeV/c	5.0 GeV/c
Material budget	9.0	9.0	9.0	9.0	9.0	9.0
Yield extraction	0.6	2.6	3.3	5.9	10.6	5.0
e^+/e^- identification	0.7	1.4	2.9	5.3	9.0	10.5
Photon identification ($\chi^2(\gamma)$)	2.4	0.9	3.7	4.6	4.0	6.7
π^0 reconstruction efficiency	0.5	3.6	3.5	4.1	6.7	8.4
Pile-up correction	1.8	1.8	2.0	2.0	–	–
Total	9.5	10.3	11.4	13.6	18.3	18.2

297 peak position and peak width was still consistent with the data. The uncertainty of the PHOS measure-
 298 ment coming from the uncertainty of the fraction of photons lost due to conversion was estimated by
 299 comparing measurements without magnetic field to the measurements with magnetic field.

300 In the PCM measurement, the main sources of systematic uncertainties include the knowledge of the
 301 material budget, raw yield extraction, electron identification (PID), the additional photon identification
 302 cuts, and π^0 reconstruction efficiency. The uncertainty related to the pile-up correction is only relevant in
 303 pp and peripheral Pb-Pb collisions. The contribution from the raw π^0 yield extraction was estimated by
 304 changing the normalization range, the integration window, and the combinatorial background evaluation.
 305 Uncertainties related to the electron and photon identification cuts, and to the photon reconstruction
 306 efficiency were estimated by evaluating the stability of the results for different cuts. The total systematic
 307 uncertainties of the PCM and the PHOS results were calculated by adding the individual contributions in
 308 quadrature.

309 The comparisons of the fully corrected π^0 spectra measured by PHOS and PCM in pp and Pb-Pb col-
 310 lisions are presented in Figs. 3 and 4, respectively. For a better comparison the ratio between the PCM
 311 and PHOS data points and the combined spectrum which was fitted with a function is shown. In all
 312 cases, agreement between the two measurements is found. The PHOS and PCM spectra were combined
 313 by calculating the average yields together with their statistical and systematic uncertainties by using the
 314 inverse squares of the total uncertainties of the PHOS and PCM measurements for a given p_T bin as
 315 respective weights [40].

316 4 Results

317 The invariant neutral pion spectra measured in pp and Pb-Pb collisions are shown in Fig. 5. The p_T range
 318 0.6 – 12 GeV/c covered by the measurements includes the region $p_T \approx 7$ GeV/c where the charged
 319 hadron R_{AA} exhibits the strongest suppression [35–37]. The invariant neutral pion yield in inelastic pp
 320 collisions shown in Fig. 5 is related to the invariant cross section as $E d^3\sigma/d^3p = E d^3N/d^3p \times \sigma_{\text{inel}}$.

321 Above $p_T \approx 3$ GeV/c the pp spectrum is well described by a power law $E d^3N/d^3p \propto 1/p_T^n$. A fit for
 322 $p_T > 3$ GeV/c yields an exponent $n = 6.0 \pm 0.1$ with $\chi^2/\text{ndf} = 3.8/4$, which is significantly smaller than
 the value $n = 8.22 \pm 0.09$ observed in pp collisions at $\sqrt{s} = 200$ GeV [31].

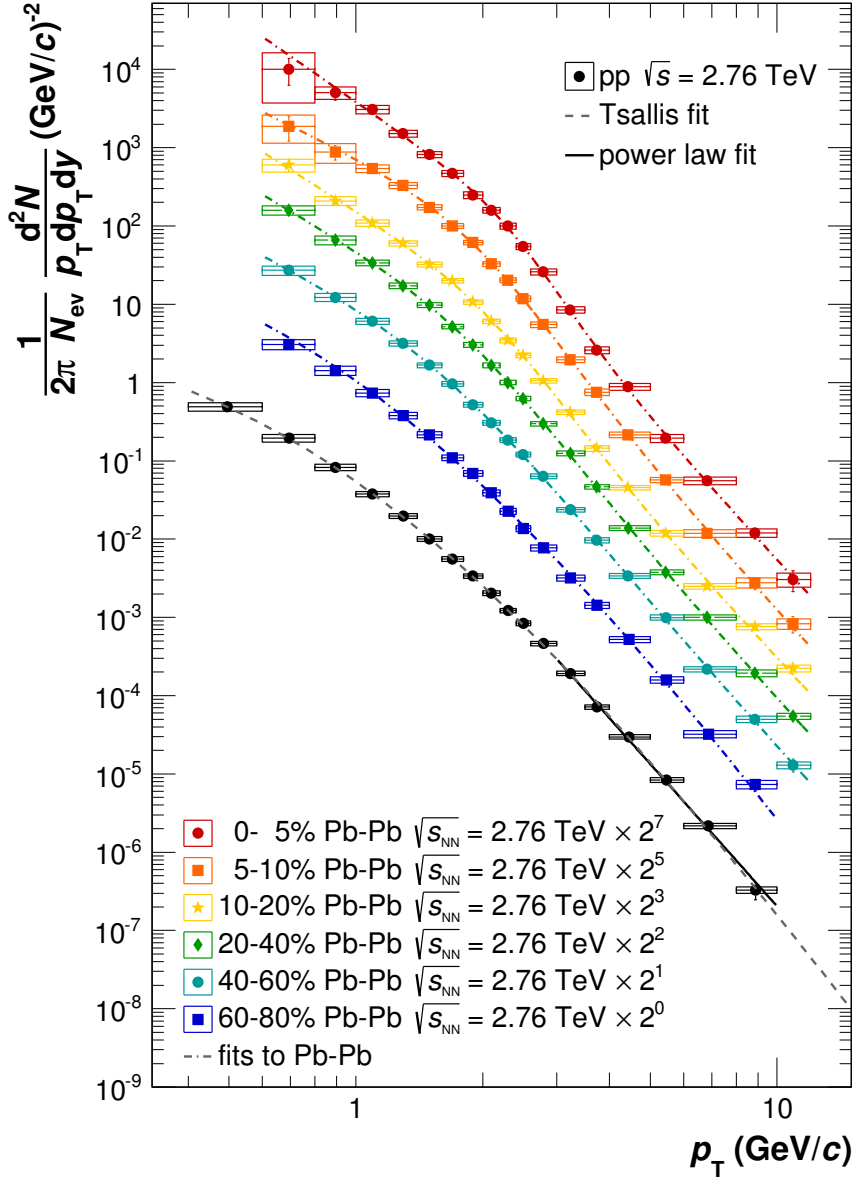


Fig. 5: (Color online) Invariant differential yields of neutral pions produced in Pb-Pb and inelastic pp collisions at $\sqrt{s_{\text{NN}}} = 2.76$ TeV. The spectra are the weighted average of the PHOS and the PCM results. The vertical lines show the statistical uncertainties, systematic uncertainties are shown as boxes. Horizontal lines indicate the bin width. The horizontal position of the data points within a bin was determined by the procedure described in [59]. For the pp spectrum a fit with a power law function $1/p_T^n$ for $p_T > 3$ GeV/c and a Tsallis function (also used in [48]) are shown. The extrapolation of the pp spectrum provided by the Tsallis fit is used in the R_{AA} calculation for $p_T \gtrsim 8$ GeV/c.

323

324 Neutral pion production from hard scattering is dominated by the fragmentation of gluon jets in the p_T
 325 range of the measurement. The presented π^0 spectrum in pp collisions can therefore help constrain the
 326 gluon-to-pion fragmentation function [61]. A next-to-leading-order (NLO) perturbative QCD calculation
 327 employing the DSS fragmentation function [62] agrees reasonably well with the measured neutral pion
 328 spectrum at $\sqrt{s} = 0.9$ TeV. At $\sqrt{s} = 7$ TeV, however, the predicted invariant cross sections are larger than

329 the measured ones [48]. The comparison to a NLO perturbative QCD calculation using the CTEQ6M5
 330 parton distributions [63] and the DSS fragmentation functions in Fig. 6 shows that the calculation over-
 331 predicts the data already at $\sqrt{s} = 2.76$ TeV by a similar factor as in pp collisions at $\sqrt{s} = 7$ TeV. The
 332 data are furthermore compared to a PYTHIA 8.176 (tune 4C) [56, 64] calculation which reproduces the
 333 shape of the spectrum with an overall offset of about 20%. It will be interesting to see whether calcula-
 334 tions in the framework of the color glass condensate [65], which describe the neutral pion spectrum in
 pp collisions at $\sqrt{s} = 7$ TeV, will also provide a good description of the data at $\sqrt{s} = 2.76$ TeV.

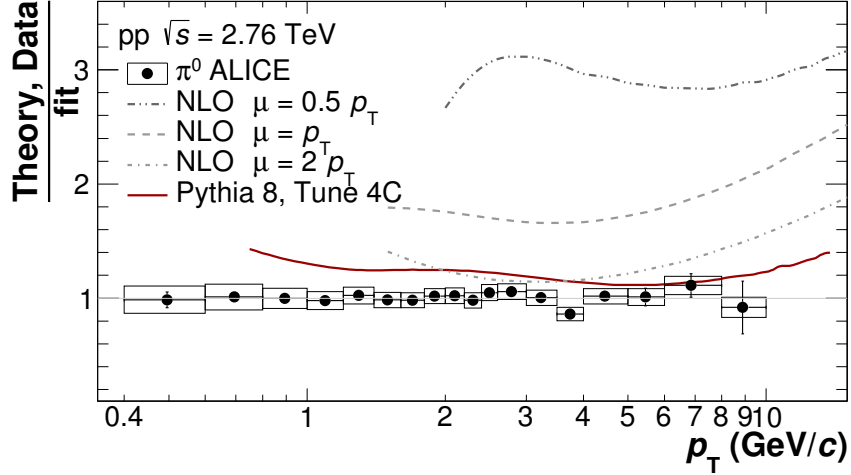


Fig. 6: (Color online) Ratio of data or theory calculations to a fit of the neutral pion spectrum in pp collisions at $\sqrt{s_{NN}} = 2.76$ TeV. The renormalization, factorization, and fragmentation scale of the next-to-leading order QCD calculation were varied simultaneously ($\mu = 0.5p_T, p_T, 2p_T$). The calculation employed the CTEQ6M5 [63] parton distribution functions and the DSS fragmentation function [62]. The solid red line is a comparison to the PYTHIA 8.176 (tune 4C) event generator [56, 64].

335

336 The nuclear modification factor, R_{AA} , was calculated according to Eq. 1. For $p_T > 8$ GeV/ c the extrap-
 337 olation of the pp spectrum provided by the Tsallis fit shown in Fig. 5 was used as reference. The average
 338 values of the nuclear overlap function T_{AA} for each centrality class were taken from [46] and are given in
 339 Table 2. They were determined with a Glauber Monte Carlo calculation [66, 67] by defining percentiles
 with respect to the simulated impact parameter b and therefore represent purely geometric quantities.

centrality class	$\langle T_{AA} \rangle$ (1/mb)	rel. syst. uncert. (%)
0-5%	26.32	3.2
5-10%	20.56	3.3
10-20%	14.39	3.1
20-40%	6.85	3.3
40-60%	1.996	4.9
60-80%	0.4174	6.2

Table 2: Values for the overlap function $\langle T_{AA} \rangle$ for the centrality bins used in this analysis.

340

341 The combined R_{AA} was calculated as a weighted average of the individual R_{AA} measured with PHOS
 342 and PCM. This has the advantage of reduced systematic uncertainties of the combined result. In partic-
 343 ular, the dominant uncertainty in the PCM, related to the material budget, cancels this way. The results
 344 for the combined R_{AA} are shown in Fig. 7. In all centrality classes the measured R_{AA} exhibits a maxi-
 345 mum around $p_T \approx 1 - 2$ GeV/ c , a decrease in the range $2 \lesssim p_T \lesssim 3 - 6$ GeV/ c , and an approximately
 346 constant value in the measured p_T range for higher p_T . For $p_T \gtrsim 6$ GeV/ c , where particle production is
 347 expected to be dominated by fragmentation of hard-scattered partons, R_{AA} decreases with centrality from
 348 about 0.5 - 0.7 in the 60 - 80% class to about 0.1 in the 0-5% class. The R_{AA} measurements for neutral

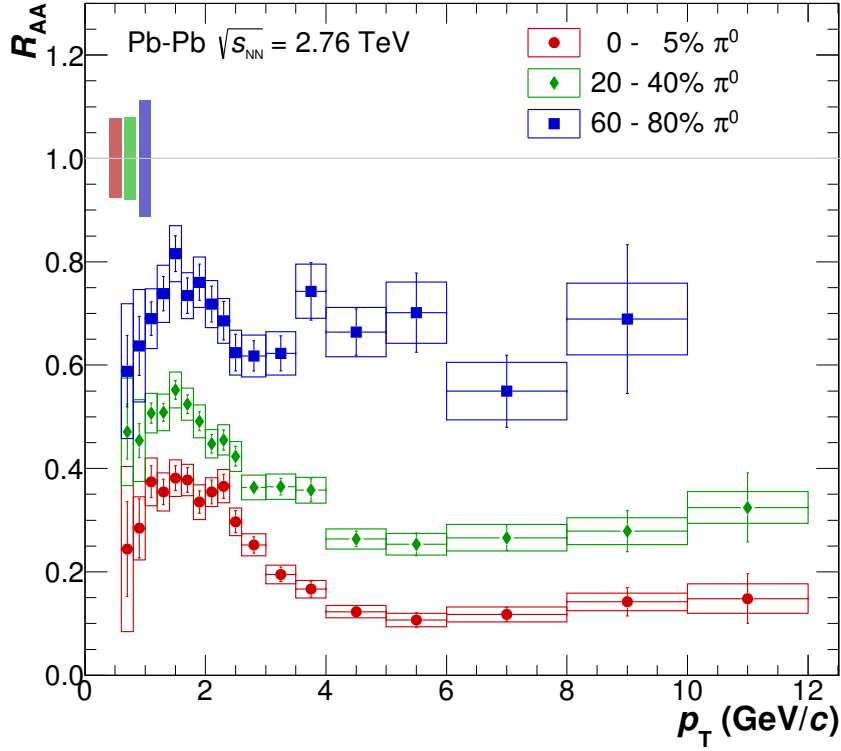


Fig. 7: (Color online) Neutral pion nuclear modification factor R_{AA} for three different centralities (0 – 5%, 20 – 40%, 60 – 80%) in Pb-Pb collisions at $\sqrt{s_{NN}} = 2.76$ TeV. Vertical error bars reflect statistical uncertainties, boxes systematic uncertainties. Horizontal bars reflect the bin width. The boxes around unity reflect the uncertainty of the average nuclear overlap function (T_{AA}) and the normalization uncertainty of the pp spectrum added in quadrature.

349 pions and charged pions [68] agree with each other over the entire p_T range for all centrality classes.
 350 Agreement between the neutral pion and charged particle R_{AA} [37] is observed for $p_T \gtrsim 6$ GeV/c.

351 It is instructive to study the $\sqrt{s_{NN}}$ dependence of the neutral pion R_{AA} . Fig. 8 shows that for central colli-
 352 sions the R_{AA} at the LHC for $p_T \gtrsim 2$ GeV/c lies below the data points at lower $\sqrt{s_{NN}}$. This indicates that
 353 the decrease of R_{AA} resulting from the higher initial energy densities created at larger $\sqrt{s_{NN}}$ dominates
 354 over the increase of R_{AA} expected from the harder initial parton p_T spectra. The shape of $R_{AA}(p_T)$ in
 355 central collisions at $\sqrt{s_{NN}} = 200$ GeV and $\sqrt{s_{NN}} = 2.76$ TeV appears to be similar. Considering the data
 356 for all shown energies one observes that the value of p_T with the maximum R_{AA} value appears to shift
 357 towards lower p_T with increasing $\sqrt{s_{NN}}$. The centrality dependence of R_{AA} at $p_T = 7$ GeV/c is shown in
 358 Fig. 9 for nuclear collisions at $\sqrt{s_{NN}} = 39, 62.4, 200$ [22, 34], and 2760 GeV. At this transverse momen-
 359 tum soft particle production from the bulk should be negligible and parton energy loss is expected to be
 360 the dominant effect. It can be seen that the suppression in Pb-Pb collisions at the LHC is stronger than in
 361 Au-Au collisions at $\sqrt{s_{NN}} = 200$ GeV for all centralities. In particular, the most peripheral class of the
 362 LHC data already shows a sizable suppression whereas at the lower energies the suppression appears to
 363 develop less abruptly as a function of the number of participating nucleons (N_{part}).

364 In Fig. 10 the measured R_{AA} is compared with a GLV model calculation [38, 39] and with theoretical
 365 predictions from the WHDG model [70]. These models describe the interaction of a hard-scattered
 366 parton with the medium of high color charge density within perturbative QCD [11]. Both calculations
 367 assume that the hadronization of the hard-scattered parton occurs in the vacuum and is not affected by the
 368 medium. They model the energy loss of the parton but not the corresponding response of the medium.
 369 Their applicability is limited to transverse momenta above 2 – 4 GeV/c as soft particle production from
 370 the bulk is not taken into account. The Pb-Pb π^0 spectra are therefore also compared to two models

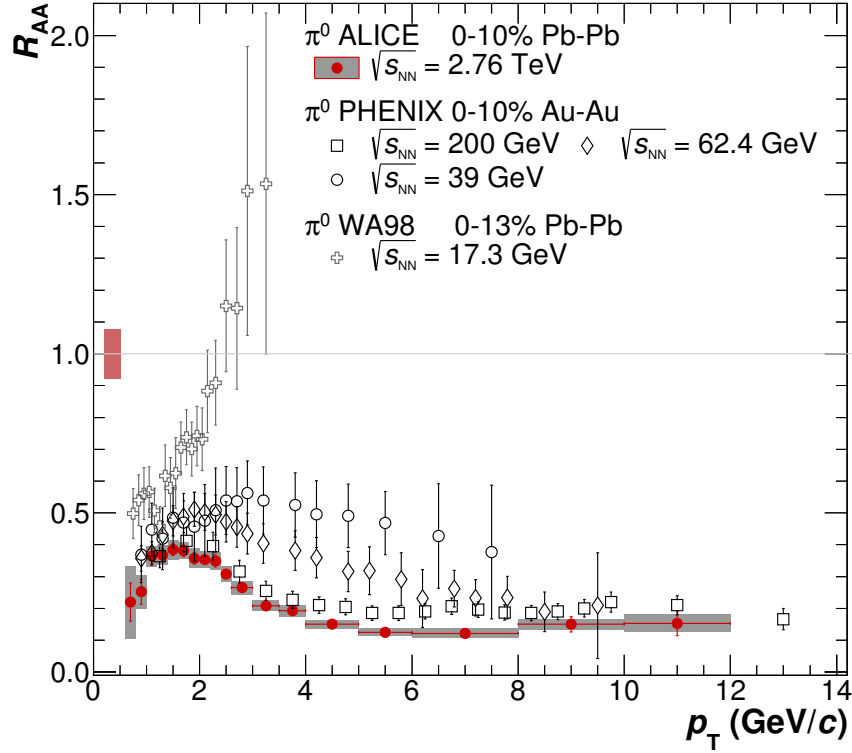


Fig. 8: (Color online) Neutral pion nuclear modification factor, R_{AA} , in Pb-Pb collisions at $\sqrt{s_{NN}} = 2.76$ TeV for the 0 – 10% class in comparison to results at lower energies. The box around unity reflects the uncertainty of the average nuclear overlap function (T_{AA}) and the normalization uncertainty of the pp spectrum added in quadrature. Horizontal bars reflect the bin width. The center-of-mass energy dependence of the neutral pion R_{AA} is shown with results from Au–Au collisions at $\sqrt{s_{NN}} = 39, 62.4$ [34], and 200 GeV [31] as well as the result from the CERN SPS [69] (using scaled p-C data as reference) along with the results for Pb-Pb at $\sqrt{s_{NN}} = 2.76$ TeV. The scale uncertainties of the measurements at lower energies of the order of 10 – 15% are not shown.

371 which aim at a description of the full p_T range: an EPOS calculation [71] and a calculation by Nemchik
 372 et al. based on the combination of a hydrodynamic description at low p_T and the absorption of color
 373 dipoles at higher p_T [72, 73]. These comparisons are presented in Fig. 11.

374 The GLV calculation takes final-state radiative energy loss into account. It includes the broadening of
 375 the transverse momenta of the incoming partons in cold nuclear matter (“nuclear broadening” or “Cronin
 376 effect”). The main parameter of this model, the initial gluon density, was tuned to describe the neutral
 377 pion suppression observed in Au-Au collisions at RHIC. For the calculation of the parton energy loss in
 378 Pb-Pb collisions at the LHC the initial gluon density was constrained by the measured charged-particle
 379 multiplicities. The model can approximately reproduce the centrality and p_T dependence of the π^0 R_{AA} .

380 The WHDG model takes into account collisional and radiative parton energy loss and geometrical path
 381 length fluctuations. The color charge density of the medium is assumed to be proportional to the number
 382 of participating nucleons from a Glauber model, and hard parton-parton scatterings are proportional
 383 to the number of binary nucleon-nucleon collisions. Parameters of the model were constrained by the
 384 neutral pion R_{AA} measured at RHIC. Like in the case of the GLV calculation, the neutral pion R_{AA} at
 385 the LHC is then predicted by translating the measured charged-particle multiplicity $dN_{ch}/d\eta$ in Pb-Pb
 386 collisions into an initial gluon density which is the free parameter of the model. For central collisions
 387 this yielded an increase in the gluon density from $dN_g/dy \approx 1400$ at RHIC to $dN_g/dy \approx 3000$ at the LHC.
 388 The WHDG model reproduces the π^0 R_{AA} in central collisions reasonably well, but predicts too strong
 389 suppression for more peripheral classes.

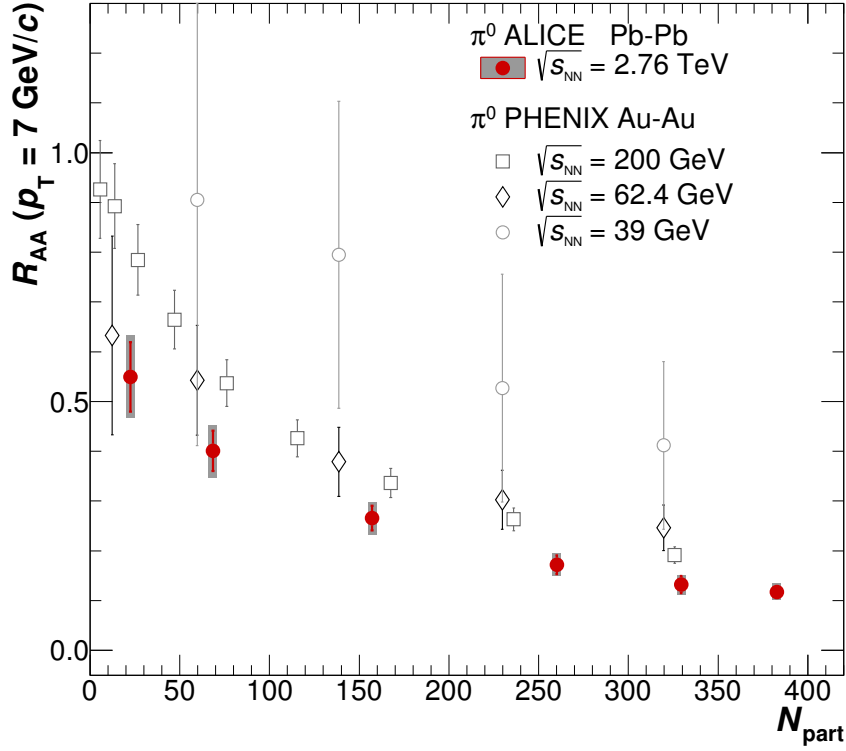


Fig. 9: (Color online) Centrality dependence of the π^0 nuclear modification factor R_{AA} at $p_T = 7$ GeV/ c in Au-Au and Pb-Pb collisions at $\sqrt{s_{NN}} = 39, 62.4, 200$ [22, 34], and 2760 GeV.

390 The two model predictions for the full p_T range are compared to the measured spectra in Fig. 11. EPOS
 391 is based on the hadronization of flux tubes produced early in the collision. Hard scattering in this model
 392 produces strings with transversely moving parts. String segments with low energies are assumed to be
 393 part of the bulk whose space-time evolution is modeled within hydrodynamics. String segments with
 394 sufficiently large energy fragment in the vacuum. A third class of string segments with intermediate
 395 energies is considered to have enough energy to leave the medium accompanied by quark pick-up from
 396 the bulk during the fragmentation process. In EPOS particle production is determined by hydrodynamic
 397 flow at low p_T ($\lesssim 4$ GeV/ c), followed at higher p_T by energy loss of high- p_T string segments. In
 398 central collisions the EPOS calculation describes the measured π^0 spectrum rather well. Towards more
 399 peripheral collisions a discrepancy develops for $1 \lesssim p_T \lesssim 5$ GeV/ c which may possibly be attributed to
 400 underestimating the contribution of hydrodynamic flow in peripheral collisions.

401 The calculation by Nemchik et al. also combines a model for hadron suppression at high p_T with a hy-
 402 drodynamic description of bulk particle production at low p_T . Hadron suppression in this model results
 403 from the absorption of pre-hadrons, i.e., of color dipoles which are already formed in the medium by
 404 hard-scattered partons during the production of hadrons with large $z = p_{hadron}/p_{parton}$. As the model, at
 405 high p_T , predicts only R_{AA} , the calculated R_{AA} values were scaled by $\langle T_{AA} \rangle \times E d^3\sigma_{meas}^{\pi^0}/d^3p$ and then
 406 added to the calculated π^0 invariant yields from the hydrodynamic model in order to compare to the
 407 measured π^0 spectra. The hydrodynamic calculation dominates the total π^0 yield up to $p_T = 2$ GeV/ c
 408 and remains a significant contribution up to 5 GeV/ c . From about 3 GeV/ c the contribution from hard
 409 scattering becomes larger than the one from the hydrodynamic calculation. The spectrum in central
 410 Pb-Pb collisions (0 – 5%) is approximately described except for the transition region between the hydro-
 411 dynamic and the hard contribution. In the 20 – 40% class the hydrodynamic calculation overpredicts the
 412 data up to $p_T = 2$ GeV/ c .

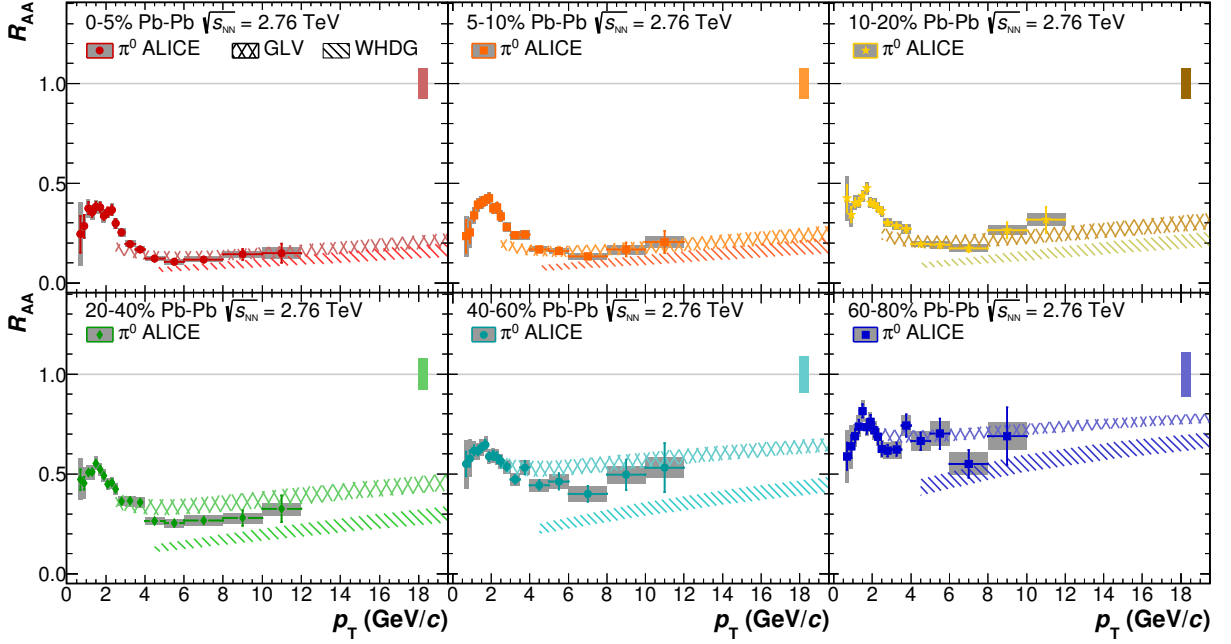


Fig. 10: (Color online) Comparison of the measured nuclear modification factor R_{AA} with a GLV calculation [38, 39] and with a WHDG [70] parton energy loss calculations. Vertical lines show the statistical uncertainties, systematic uncertainties are shown as boxes. Horizontal lines indicate the bin width. The boxes around unity reflect the scale uncertainties of data related to T_{AA} and the normalization of the pp spectrum.

5 Conclusions

Measurements of neutral pion production at midrapidity in pp and Pb-Pb collisions at $\sqrt{s_{NN}} = 2.76$ TeV were presented. The measurements were performed with two independent techniques, by measuring the photons with the electromagnetic calorimeter PHOS, and by measuring converted photons with the ALICE tracking system. The two independent measurements were found to give consistent results, and were combined for the final results.

The neutral pion spectrum in pp collisions was compared to a NLO perturbative QCD calculation using the DSS fragmentation functions. This calculation, which describes the pion spectrum in pp collisions at $\sqrt{s} = 0.9$ TeV rather well, tends to overpredict the π^0 cross section already at $\sqrt{s} = 2.76$ TeV. Along with a similar observation in pp collision at $\sqrt{s} = 7$ TeV this indicates the likely need for improvements in the gluon-to-pion fragmentation function. As similar observation was made for transverse momentum spectra of charged particles in proton-proton and proton-antiproton collisions at $1.96 \lesssim \sqrt{s} \lesssim 7$ TeV [61, 74].

The neutral pion nuclear suppression factor R_{AA} was calculated from the measured neutral pion spectra, and was compared to measurements at lower energies and to theoretical predictions. The π^0 suppression in the most central class (0 – 5%) reaches values of up to 8 – 10 for $5 \lesssim p_T \lesssim 7$ GeV/c. The suppression in Pb-Pb collisions at $\sqrt{s_{NN}} = 2.76$ TeV is stronger than in Au-Au collisions at $\sqrt{s_{NN}} = 200$ GeV (and lower energies) at RHIC for all centralities.

The general features of the centrality and p_T dependence of the R_{AA} for $p_T \gtrsim 2$ GeV/c are approximately reproduced by GLV and WHDG parton energy loss calculations, although the WHDG calculation performs less well in peripheral collisions. For both calculations the main free parameter, the initial gluon density, was chosen to describe the neutral pion suppression at RHIC and then scaled to LHC energies based on the measured charged-particle multiplicities. The measured π^0 spectra were also compared to calculations with the EPOS event generator and a calculation by Nemchik et al. By combining soft particle production from a hydrodynamically evolving medium with a model for hadron suppression these

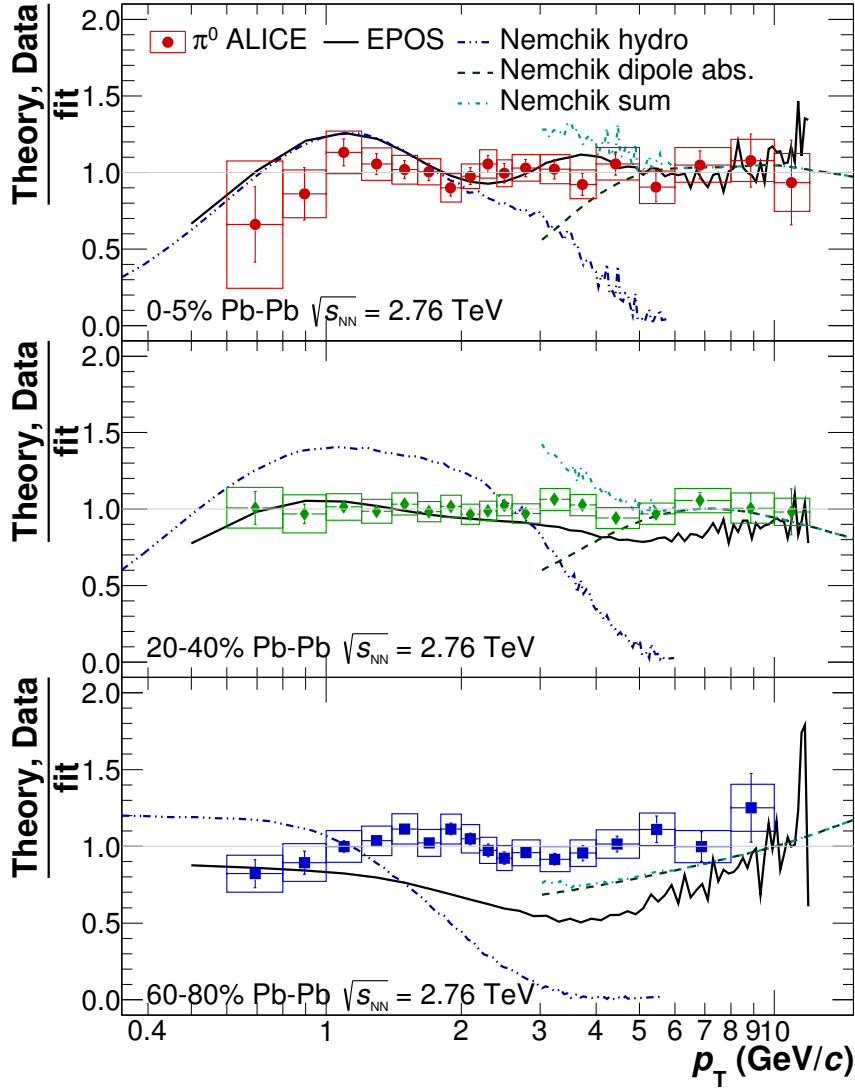


Fig. 11: (Color online) Comparison of the measured π^0 spectra for three centrality classes (0 – 5%, 20 – 40%, 60 – 80%) with two calculations which make predictions for the full p_T range of the measurement. The calculated spectra and the data points were divided by a fit of the measured π^0 spectra. For the data points the error bars represent the statistical uncertainties and the boxes the systematic uncertainties. Calculations with the EPOS event generator [71] are shown by the solid line. The fluctuations of the EPOS lines at high p_T are due to limited statistics in the number of generated events. The calculations by Nemchik et al. [72,73] combine a hydrodynamical model at low p_T with a color dipole absorption model for $p_T \gtrsim 3$ GeV/ c . The two components and the sum (for $p_T \gtrsim 3$ GeV/ c) are shown separately.

438 models are capable of making predictions for the entire p_T range. An important task on the theoretical
 439 side will be to establish whether the observed deviations from the data simply indicate a suboptimal ad-
 440 justment of parameters or hint at important physical phenomena missing in the models. Future analyses
 441 based on runs with higher integrated luminosities, e.g. the 2011 LHC Pb-Pb run, will also include the
 442 ALICE lead-scintillator electromagnetic calorimeter (EMCal) and will allow us to extend the neutral pion
 443 measurement to higher transverse momenta. The role of initial-state effects on the particle production in
 444 Pb-Pb collisions will be investigated by measurements of particle production in p-Pb collisions.

system	A	C (MeV/c ²)	n
pp	1.7 ± 0.7	135 ± 29	7.1 ± 0.7
60 – 80% Pb-Pb	31.7	142	7.4

Table 3: Parameters of the fits of the Tsallis parameterization (Eq. 3) to the combined invariant production yields for π^0 mesons in inelastic collisions at $\sqrt{s} = 2.76$ TeV. The uncertainties (statistical and systematic added in quadrature) were used to evaluate the uncertainty of the extrapolation used in the calculation of R_{AA} for $p_T > 8$ GeV/c. The uncertainty on the parameter A due to the spectra normalization of 3.9% at $\sqrt{s} = 2.76$ TeV is not included. For the measurement in 60 – 80% Pb-Pb collisions the fit parameters are given without uncertainties as the parameterization is only used to facilitate the comparison with model calculations.

centrality	a	b	c	d	e
0 – 5%	28.96	5.85	-199.17	4.64	95.30
5 – 10%	21.97	5.79	-33.54	2.96	10.84
0 – 10%	25.53	5.84	-49.95	3.35	18.49
10 – 20%	18.91	5.71	-44.76	3.37	19.66
20 – 40%	11.54	5.74	-18.43	2.62	7.37
40 – 60%	4.18	5.67	-9.43	2.00	3.39

Table 4: Parameters of the fits to the combined invariant yields of π^0 mesons in Pb-Pb collisions in different centrality classes with the functional form given in Eq. 4. The spectra were fitted taking into account the combined statistical and systematic errors.

445 Appendix

446 For the calculation of the R_{AA} above $p_T > 8$ GeV/c an extrapolation of the measured transverse momen-
447 tum spectrum in pp collisions at $\sqrt{s} = 2.76$ TeV based on the Tsallis functional form

$$\frac{1}{2\pi p_T} \frac{d^2N}{dp_T dy} = \frac{A}{2\pi nC} \frac{(n-1)(n-2)}{[nC + m(n-2)]} \cdot \left(1 + \frac{\sqrt{p_T^2 + m^2} - m}{nC} \right)^{-n} \quad (3)$$

448 was used (where m is the mass of the neutral pion). The parameters are given in Table 3.

449 In order to compare the individual PCM and PHOS measurements to the combined results in Pb-Pb col-
450 lisions the parameterization

$$\frac{1}{2\pi p_T} \frac{d^2N}{dp_T dy} = a \cdot p_T^{-(b+c/(p_T^d+e))} \quad (4)$$

451 was used to fit the combined spectrum for each centrality class. The corresponding parameters are given
452 in Tab. 4. For the most peripheral centrality class the Tsallis parameterization Eq. 3 was used for which
453 the parameters are given in Tab. 3. These parameterizations describe the data well in the measured
454 momentum range.

455 Acknowledgements

456 We would like to thank Jan Nemchik, William A. Horowitz, Ivan Vitev, and Klaus Werner for providing
457 the model calculations shown in this paper. This work was supported by the grants RFBR 10-02-91052
458 and RFBR 12-02-91527. The ALICE Collaboration would like to thank all its engineers and technicians
459 for their invaluable contributions to the construction of the experiment and the CERN accelerator teams
460 for the outstanding performance of the LHC complex.

461 The ALICE Collaboration gratefully acknowledges the resources and support provided by all Grid cen-
462 tres and the Worldwide LHC Computing Grid (WLCG) collaboration.

463 The ALICE Collaboration acknowledges the following funding agencies for their support in building and
464 running the ALICE detector:

465 State Committee of Science, World Federation of Scientists (WFS) and Swiss Fonds Kidagan, Armenia,
466 Conselho Nacional de Desenvolvimento Científico e Tecnológico (CNPq), Financiadora de Estudos e
467 Projetos (FINEP), Fundação de Amparo à Pesquisa do Estado de São Paulo (FAPESP);
468 National Natural Science Foundation of China (NSFC), the Chinese Ministry of Education (CMOE) and
469 the Ministry of Science and Technology of China (MSTC);
470 Ministry of Education and Youth of the Czech Republic;
471 Danish Natural Science Research Council, the Carlsberg Foundation and the Danish National Research
472 Foundation;

473 The European Research Council under the European Community's Seventh Framework Programme;
474 Helsinki Institute of Physics and the Academy of Finland;

475 French CNRS-IN2P3, the 'Region Pays de Loire', 'Region Alsace', 'Region Auvergne' and CEA,
476 France;

477 German BMBF and the Helmholtz Association;

478 General Secretariat for Research and Technology, Ministry of Development, Greece;

479 Hungarian OTKA and National Office for Research and Technology (NKTH);

480 Department of Atomic Energy and Department of Science and Technology of the Government of India;

481 Istituto Nazionale di Fisica Nucleare (INFN) and Centro Fermi - Museo Storico della Fisica e Centro
482 Studi e Ricerche "Enrico Fermi", Italy;

483 MEXT Grant-in-Aid for Specially Promoted Research, Japan;

484 Joint Institute for Nuclear Research, Dubna;

485 National Research Foundation of Korea (NRF);

486 CONACYT, DGAPA, México, ALFA-EC and the EPLANET Program (European Particle Physics Latin
487 American Network)

488 Stichting voor Fundamenteel Onderzoek der Materie (FOM) and the Nederlandse Organisatie voor
489 Wetenschappelijk Onderzoek (NWO), Netherlands;

490 Research Council of Norway (NFR);

491 Polish Ministry of Science and Higher Education;

492 National Science Centre, Poland;

493 Ministry of National Education/Institute for Atomic Physics and CNCS-UEFISCDI - Romania;

494 Ministry of Education and Science of Russian Federation, Russian Academy of Sciences, Russian Fed-
495 eral Agency of Atomic Energy, Russian Federal Agency for Science and Innovations and The Russian
496 Foundation for Basic Research;

497 Ministry of Education of Slovakia;

498 Department of Science and Technology, South Africa;

499 CIEMAT, EELA, Ministerio de Economía y Competitividad (MINECO) of Spain, Xunta de Galicia
500 (Consellería de Educación), CEADEN, Cubaenergía, Cuba, and IAEA (International Atomic Energy
501 Agency);

502 Swedish Research Council (VR) and Knut & Alice Wallenberg Foundation (KAW);

503 Ukraine Ministry of Education and Science;

504 United Kingdom Science and Technology Facilities Council (STFC);

505 The United States Department of Energy, the United States National Science Foundation, the State of
506 Texas, and the State of Ohio.

507

508 **References**

- 509 [1] S. Borsanyi *et al.*, JHEP **1011**, 077 (2010), 1007.2580.
510 [2] A. Bazavov *et al.*, Phys.Rev. **D85**, 054503 (2012), 1111.1710.
511 [3] CMS Collaboration, S. Chatrchyan *et al.*, Phys.Rev.Lett. **109**, 152303 (2012), 1205.2488.
512 [4] A. Toia, J.Phys.G **G38**, 124007 (2011), 1107.1973.
513 [5] U. Heinz and R. Snellings, Ann.Rev.Nucl.Part.Sci. **63**, 123 (2013), 1301.2826.
514 [6] J. Bjorken, (1982), FERMILAB-PUB-82-059-THY, FERMILAB-PUB-82-059-T.
515 [7] X.-N. Wang and M. Gyulassy, Phys.Rev.Lett. **68**, 1480 (1992).
516 [8] U. A. Wiedemann, Jet Quenching in Heavy Ion Collisions, in *SpringerMaterials - The Landolt-
517 Börnstein Database*, edited by R. Stock Vol. 23: Relativistic Heavy Ion Physics, Springer-Verlag
518 Berlin Heidelberg, 2009, 0908.2306.
519 [9] D. d’Enterria, Jet quenching, in *SpringerMaterials - The Landolt-Börnstein Database*, edited
520 by R. Stock Vol. 23: Relativistic Heavy Ion Physics, Springer-Verlag Berlin Heidelberg, 2009,
521 0902.2011.
522 [10] A. Majumder and M. Van Leeuwen, Prog.Part.Nucl.Phys. **A66**, 41 (2011), 1002.2206.
523 [11] N. Armesto *et al.*, Phys.Rev. **C86**, 064904 (2012), 1106.1106.
524 [12] K. M. Burke *et al.*, (2013), 1312.5003.
525 [13] ALICE Collaboration, B. Abelev *et al.*, Phys.Rev.Lett. **110**, 082302 (2013), 1210.4520.
526 [14] W. Horowitz and M. Gyulassy, Nucl.Phys. **A872**, 265 (2011), 1104.4958.
527 [15] R. Sassot, P. Zurita, and M. Stratmann, Phys.Rev. **D82**, 074011 (2010), 1008.0540.
528 [16] R. Sassot, M. Stratmann, and P. Zurita, Phys.Rev. **D81**, 054001 (2010), 0912.1311.
529 [17] S. Sapeta and U. A. Wiedemann, Eur.Phys.J. **C55**, 293 (2008), 0707.3494.
530 [18] R. Bellwied and C. Markert, Phys.Lett. **B691**, 208 (2010), 1005.5416.
531 [19] PHENIX Collaboration, K. Adcox *et al.*, Phys.Rev.Lett. **88**, 022301 (2002), nucl-ex/0109003.
532 [20] STAR Collaboration, C. Adler *et al.*, Phys.Rev.Lett. **89**, 202301 (2002), nucl-ex/0206011.
533 [21] STAR Collaboration, G. Agakishiev *et al.*, Phys.Rev.Lett. **108**, 072302 (2012), 1110.0579.
534 [22] PHENIX Collaboration, A. Adare *et al.*, Phys.Rev. **C87**, 034911 (2013), 1208.2254.
535 [23] PHENIX Collaboration, A. Adare *et al.*, Phys.Rev. **C88**, 024906 (2013), 1304.3410.
536 [24] STAR Collaboration, C. Adler *et al.*, Phys.Rev.Lett. **90**, 082302 (2003), nucl-ex/0210033.
537 [25] STAR Collaboration, J. Adams *et al.*, Phys.Rev.Lett. **97**, 162301 (2006), nucl-ex/0604018.
538 [26] BRAHMS Collaboration, I. Arsene *et al.*, Nucl.Phys. **A757**, 1 (2005), nucl-ex/0410020.
539 [27] PHENIX Collaboration, K. Adcox *et al.*, Nucl.Phys. **A757**, 184 (2005), nucl-ex/0410003.
540 [28] B. Back *et al.*, Nucl.Phys. **A757**, 28 (2005), nucl-ex/0410022.
541 [29] STAR Collaboration, J. Adams *et al.*, Nucl.Phys. **A757**, 102 (2005), nucl-ex/0501009.
542 [30] PHENIX Collaboration, S. Adler *et al.*, Phys.Rev.Lett. **91**, 072301 (2003), nucl-ex/0304022.
543 [31] PHENIX Collaboration, A. Adare *et al.*, Phys.Rev.Lett. **101**, 232301 (2008), 0801.4020.
544 [32] S. A. Bass *et al.*, Phys.Rev. **C79**, 024901 (2009), 0808.0908.
545 [33] PHENIX Collaboration, A. Adare *et al.*, Phys.Rev.Lett. **101**, 162301 (2008), 0801.4555.
546 [34] PHENIX Collaboration, A. Adare *et al.*, Phys.Rev.Lett. **109**, 152301 (2012), 1204.1526.
547 [35] ALICE Collaboration, K. Aamodt *et al.*, Phys.Lett. **B696**, 30 (2011), 1012.1004.
548 [36] CMS Collaboration, S. Chatrchyan *et al.*, Eur.Phys.J. **C72**, 1945 (2012), 1202.2554.
549 [37] ALICE Collaboration, B. Abelev *et al.*, Phys.Lett. **B720**, 52 (2013), 1208.2711.
550 [38] R. Sharma, I. Vitev, and B.-W. Zhang, Phys.Rev. **C80**, 054902 (2009), 0904.0032.
551 [39] R. Neufeld, I. Vitev, and B.-W. Zhang, Phys.Lett. **B704**, 590 (2011), 1010.3708.

- 552 [40] Particle Data Group, J. Beringer *et al.*, Phys.Rev. **D86**, 010001 (2012).
- 553 [41] ALICE Collaboration, G. Dellacasa *et al.*, CERN-LHCC-99-04 (1999).
- 554 [42] ALICE Collaboration, K. Aamodt *et al.*, JINST **5**, P03003 (2010), 1001.0502.
- 555 [43] J. Alme *et al.*, Nucl.Instrum.Meth. **A622**, 316 (2010), 1001.1950.
- 556 [44] ALICE Collaboration, K. Aamodt *et al.*, JINST **3**, S08002 (2008).
- 557 [45] ALICE Collaboration, P. Cortese *et al.*, CERN-LHCC-2004-025 (2004).
- 558 [46] ALICE Collaboration, B. Abelev *et al.*, Phys.Rev. **C88**, 044909 (2013), 1301.4361.
- 559 [47] ALICE Collaboration, B. Abelev *et al.*, Eur.Phys.J. **C73**, 2456 (2013), 1208.4968.
- 560 [48] ALICE Collaboration, B. Abelev *et al.*, Phys.Lett. **B717**, 162 (2012), 1205.5724.
- 561 [49] ALICE Collaboration, B. B. Abelev *et al.*, (2014), 1402.4476.
- 562 [50] R. Brun, F. Bruyant, M. Maire, A. McPherson, and P. Zanmarini, CERN Report No. CERN-DD-EE-
563 84-1, 1987 (unpublished).
- 564 [51] ALICE Collaboration, E. Alessandro, G *et al.*, J.Phys.G **G32**, 1295 (2006).
- 565 [52] S. Gorbunov and I. Kisel, CBM experiment Report No. CBM-SOFT-note-2007-003, 2007 (unpub-
566 lished).
- 567 [53] J. Podolanski and R. Armenteros, Philosophical Magazine **45**, 13 (1954).
- 568 [54] M. J. Oreglia, *A Study of the Reactions $\psi' \rightarrow \gamma\gamma\psi$* , PhD thesis, SLAC, Stanford University,
569 Stanford, California 94305, 1980.
- 570 [55] ALICE Collaboration, K. Koch, Nucl.Phys.A **855**, 281 (2011).
- 571 [56] T. Sjostrand, S. Mrenna, and P. Z. Skands, Comput.Phys.Commun. **178**, 852 (2008), 0710.3820.
- 572 [57] R. Engel, J. Ranft, and S. Roesler, Phys.Rev. **D52**, 1459 (1995), hep-ph/9502319.
- 573 [58] M. Gyulassy and X.-N. Wang, Comput.Phys.Commun. **83**, 307 (1994), nucl-th/9502021.
- 574 [59] G. Lafferty and T. Wyatt, Nucl.Instrum.Meth. **A355**, 541 (1995).
- 575 [60] ALICE Collaboration, B. B. Abelev *et al.*, Phys.Rev.Lett. **111**, 222301 (2013), 1307.5530.
- 576 [61] D. d'Enterria, K. J. Eskola, I. Helenius, and H. Paukkunen, Nucl.Phys. **B883**, 615 (2013),
577 1311.1415.
- 578 [62] D. de Florian, R. Sassot, and M. Stratmann, Phys.Rev. **D75**, 114010 (2007), hep-ph/0703242.
- 579 [63] J. Pumplin *et al.*, JHEP **0207**, 012 (2002), hep-ph/0201195.
- 580 [64] R. Corke and T. Sjostrand, JHEP **1103**, 032 (2011), 1011.1759.
- 581 [65] T. Lappi and H. Mntysaari, Phys.Rev. **D88**, 114020 (2013), 1309.6963.
- 582 [66] M. L. Miller, K. Reygers, S. J. Sanders, and P. Steinberg, Ann.Rev.Nucl.Part.Sci. **57**, 205 (2007),
583 nucl-ex/0701025.
- 584 [67] B. Alver, M. Baker, C. Loizides, and P. Steinberg, (2008), 0805.4411.
- 585 [68] ALICE Collaboration, B. B. Abelev *et al.*, (2014), 1401.1250.
- 586 [69] WA98 Collaboration, M. Aggarwal *et al.*, Phys.Rev.Lett. **100**, 242301 (2008), 0708.2630.
- 587 [70] W. A. Horowitz, Int.J.Mod.Phys. **E16**, 2193 (2007), nucl-th/0702084.
- 588 [71] K. Werner, I. Karpenko, M. Bleicher, T. Pierog, and S. Porteboeuf-Houssais, Phys.Rev. **C85**,
589 064907 (2012), 1203.5704.
- 590 [72] B. Kopeliovich, J. Nemchik, I. Potashnikova, and I. Schmidt, Phys.Rev. **C86**, 054904 (2012),
591 1208.4951.
- 592 [73] J. Nemchik, I. A. Karpenko, B. Kopeliovich, I. Potashnikova, and Y. M. Sinyukov, (2013),
593 1310.3455.
- 594 [74] ALICE Collaboration, B. B. Abelev *et al.*, Eur.Phys.J. **C73**, 2662 (2013), 1307.1093.

595 **A The ALICE Collaboration**

596 B. Abelev⁶⁹, J. Adam³⁷, D. Adamová⁷⁷, M.M. Aggarwal⁸¹, M. Agnello^{105,88}, A. Agostinelli²⁶, N. Agrawal⁴⁴,
597 Z. Ahammed¹²⁴, N. Ahmad¹⁸, I. Ahmed¹⁵, S.U. Ahn⁶², S.A. Ahn⁶², I. Aimo^{105,88}, S. Aiola¹²⁹, M. Ajaz¹⁵,
598 A. Akindinov⁵³, S.N. Alam¹²⁴, D. Aleksandrov⁹⁴, B. Alessandro¹⁰⁵, D. Alexandre⁹⁶, A. Alici^{12,99}, A. Alkin³,
599 J. Alme³⁵, T. Alt³⁹, S. Altinpinar¹⁷, I. Altsybeev¹²³, C. Alves Garcia Prado¹¹³, C. Andrei⁷², A. Andronic⁹¹,
600 V. Anguelov⁸⁷, J. Anielski⁴⁹, T. Antičić⁹², F. Antinori¹⁰², P. Antonioli⁹⁹, L. Aphecetche¹⁰⁷,
601 H. Appelshäuser⁴⁸, S. Arcelli²⁶, N. Armesto¹⁶, R. Arnaldi¹⁰⁵, T. Aronsson¹²⁹, I.C. Arsene⁹¹, M. Arslanok⁴⁸,
602 A. Augustinus³⁴, R. Averbeck⁹¹, T.C. Awes⁷⁸, M.D. Azmi⁸³, M. Bach³⁹, A. Badalà¹⁰¹, Y.W. Baek^{64,40},
603 S. Bagnasco¹⁰⁵, R. Bailhache⁴⁸, R. Bala⁸⁴, A. Baldisseri¹⁴, F. Baltasar Dos Santos Pedrosa³⁴, R.C. Baral⁵⁶,
604 R. Barbera²⁷, F. Barile³¹, G.G. Barnaföldi¹²⁸, L.S. Barnby⁹⁶, V. Barret⁶⁴, J. Bartke¹¹⁰, M. Basile²⁶,
605 N. Bastid⁶⁴, S. Basu¹²⁴, B. Bathen⁴⁹, G. Batigne¹⁰⁷, B. Batyunya⁶¹, P.C. Batzing²¹, C. Baumann⁴⁸,
606 I.G. Bearden⁷⁴, H. Beck⁴⁸, C. Bedda⁸⁸, N.K. Behera⁴⁴, I. Belikov⁵⁰, F. Bellini²⁶, R. Bellwied¹¹⁵,
607 E. Belmont-Moreno⁵⁹, R. Belmont III¹²⁷, V. Belyaev⁷⁰, G. Bencedi¹²⁸, S. Beole²⁵, I. Berceanu⁷²,
608 A. Bercuci⁷², Y. Berdnikov^{ii,79}, D. Berenyi¹²⁸, M.E. Berger⁸⁶, R.A. Bertens⁵², D. Berzano²⁵, L. Betev³⁴,
609 A. Bhasin⁸⁴, I.R. Bhat⁸⁴, A.K. Bhati⁸¹, B. Bhattacharjee⁴¹, J. Bhom¹²⁰, L. Bianchi²⁵, N. Bianchi⁶⁶,
610 C. Bianchin⁵², J. Bielčik³⁷, J. Bielčiková⁷⁷, A. Bilandzic⁷⁴, S. Bjelogrić⁵², F. Blanco¹⁰, D. Blau⁹⁴,
611 C. Blume⁴⁸, F. Bock^{87,68}, A. Bogdanov⁷⁰, H. Bøggild⁷⁴, M. Bogolyubsky¹⁰⁶, F.V. Böhmer⁸⁶, L. Boldizsár¹²⁸,
612 M. Bombara³⁸, J. Book⁴⁸, H. Borel¹⁴, A. Borissov^{90,127}, F. Bossú⁶⁰, M. Botje⁷⁵, E. Botta²⁵, S. Böttger⁴⁷,
613 P. Braun-Munzinger⁹¹, M. Bregant¹¹³, T. Breitner⁴⁷, T.A. Broker⁴⁸, T.A. Browning⁸⁹, M. Broz³⁷, E. Bruna¹⁰⁵,
614 G.E. Bruno³¹, D. Budnikov⁹³, H. Buesching⁴⁸, S. Bufalino¹⁰⁵, P. Buncic³⁴, O. Busch⁸⁷, Z. Buthelezi⁶⁰,
615 D. Caffarri²⁸, X. Cai⁷, H. Caines¹²⁹, L. Calero Diaz⁶⁶, A. Caliva⁵², E. Calvo Villar⁹⁷, P. Camerini²⁴,
616 F. Carena³⁴, W. Carena³⁴, J. Castillo Castellanos¹⁴, E.A.R. Casula²³, V. Catanescu⁷², C. Cavicchioli³⁴,
617 C. Ceballos Sanchez⁹, J. Cepila³⁷, P. Cerello¹⁰⁵, B. Chang¹¹⁶, S. Chapeland³⁴, J.L. Charvet¹⁴,
618 S. Chattopadhyay¹²⁴, S. Chattopadhyay⁹⁵, V. Chelnokov³, M. Cherney⁸⁰, C. Cheshkov¹²², B. Cheynis¹²²,
619 V. Chibante Barroso³⁴, D.D. Chinellato¹¹⁵, P. Chochula³⁴, M. Chojnacki⁷⁴, S. Choudhury¹²⁴,
620 P. Christakoglou⁷⁵, C.H. Christensen⁷⁴, P. Christiansen³², T. Chujo¹²⁰, S.U. Chung⁹⁰, C. Cicalo¹⁰⁰,
621 L. Cifarelli^{26,12}, F. Cindolo⁹⁹, J. Cleymans⁸³, F. Colamaria³¹, D. Colella³¹, A. Collu²³, M. Colocci²⁶,
622 G. Conesa Balbastre⁶⁵, Z. Conesa del Valle⁴⁶, M.E. Connors¹²⁹, J.G. Contreras¹¹, T.M. Cormier¹²⁷,
623 Y. Corrales Morales²⁵, P. Cortese³⁰, I. Cortés Maldonado², M.R. Cosentino¹¹³, F. Costa³⁴, P. Crochet⁶⁴,
624 R. Cruz Albino¹¹, E. Cuautle⁵⁸, L. Cunqueiro⁶⁶, A. Dainese¹⁰², R. Dang⁷, A. Danu⁵⁷, D. Das⁹⁵, I. Das⁴⁶,
625 K. Das⁹⁵, S. Das⁴, A. Dash¹¹⁴, S. Dash⁴⁴, S. De¹²⁴, H. Delagrangé^{107,1}, A. Deloff⁷¹, E. Dénes¹²⁸,
626 G. D'Erasmus³¹, A. De Caro^{29,12}, G. de Cataldo⁹⁸, J. de Cuveland³⁹, A. De Falco²³, D. De Gruttola^{29,12},
627 N. De Marco¹⁰⁵, S. De Pasquale²⁹, R. de Rooij⁵², M.A. Diaz Corchero¹⁰, T. Dietel⁴⁹, P. Dillenseger⁴⁸,
628 R. Divià³⁴, D. Di Bari³¹, S. Di Liberto¹⁰³, A. Di Mauro³⁴, P. Di Nezza⁶⁶, Ø. Djuvsland¹⁷, A. Dobrin⁵²,
629 T. Dobrowolski⁷¹, D. Domenicis Gimenez¹¹³, B. Dönigus⁴⁸, O. Dordic²¹, S. Dørheim⁸⁶, A.K. Dubey¹²⁴,
630 A. Dubla⁵², L. Ducroux¹²², P. Dupieux⁶⁴, A.K. Dutta Majumdar⁹⁵, T. E. Hilden⁴², R.J. Ehlers¹²⁹, D. Elia⁹⁸,
631 H. Engel⁴⁷, B. Erazmus^{34,107}, H.A. Erdal³⁵, D. Eschweiler³⁹, B. Espagnon⁴⁶, M. Esposito³⁴, M. Estienne¹⁰⁷,
632 S. Esumi¹²⁰, D. Evans⁹⁶, S. Evdokimov¹⁰⁶, D. Fabris¹⁰², J. Faivre⁶⁵, D. Falchieri²⁶, A. Fantoni⁶⁶, M. Fasel⁸⁷,
633 D. Fehlfker¹⁷, L. Feldkamp⁴⁹, D. Felea⁵⁷, A. Feliciello¹⁰⁵, G. Feofilov¹²³, J. Ferencei⁷⁷, A. Fernández Téllez²,
634 E.G. Ferreira¹⁶, A. Ferretti²⁵, A. Festanti²⁸, J. Figiel¹¹⁰, M.A.S. Figueredo¹¹⁷, S. Filchagin⁹³, D. Finogeev⁵¹,
635 F.M. Fionda³¹, E.M. Fiore³¹, E. Floratos⁸², M. Floris³⁴, S. Foertsch⁶⁰, P. Foka⁹¹, S. Fokin⁹⁴,
636 E. Fragaicomio¹⁰⁴, A. Francescon^{34,28}, U. Frankenfeld⁹¹, U. Fuchs³⁴, C. Furget⁶⁵, M. Fusco Girard²⁹,
637 J.J. Gaardhøje⁷⁴, M. Gagliardi²⁵, A.M. Gago⁹⁷, M. Gallio²⁵, D.R. Gangadharan¹⁹, P. Ganoti⁷⁸,
638 C. Garabatos⁹¹, E. Garcia-Solis¹³, C. Gargiulo³⁴, I. Garishvili⁶⁹, J. Gerhard³⁹, M. Germain¹⁰⁷, A. Gheata³⁴,
639 M. Gheata^{34,57}, B. Ghidini³¹, P. Ghosh¹²⁴, S.K. Ghosh⁴, P. Gianotti⁶⁶, P. Giubellino³⁴,
640 E. Gladysz-Dziadus¹¹⁰, P. Glässel⁸⁷, A. Gomez Ramirez⁴⁷, P. González-Zamora¹⁰, S. Gorbunov³⁹,
641 L. Görlich¹¹⁰, S. Gotovac¹⁰⁹, L.K. Graczykowski¹²⁶, A. Grelli⁵², A. Grigoras³⁴, C. Grigoras³⁴, V. Grigoriev⁷⁰,
642 A. Grigoryan¹, S. Grigoryan⁶¹, B. Grinyov³, N. Grion¹⁰⁴, J.F. Grosse-Oetringhaus³⁴, J.-Y. Grossiord¹²²,
643 R. Grosso³⁴, F. Guber⁵¹, R. Guernane⁶⁵, B. Guerzoni²⁶, M. Guilbaud¹²², K. Gulbrandsen⁷⁴, H. Gulkanyan¹,
644 M. Gumbo⁸³, T. Gunji¹¹⁹, A. Gupta⁸⁴, R. Gupta⁸⁴, K. H. Khan¹⁵, R. Haake⁴⁹, Ø. Haaland¹⁷, C. Hadjidakis⁴⁶,
645 M. Haiduc⁵⁷, H. Hamagaki¹¹⁹, G. Hamar¹²⁸, L.D. Hanratty⁹⁶, A. Hansen⁷⁴, J.W. Harris¹²⁹, H. Hartmann³⁹,
646 A. Harton¹³, D. Hatzifotiadou⁹⁹, S. Hayashi¹¹⁹, S.T. Heckel⁴⁸, M. Heide⁴⁹, H. Helstrup³⁵, A. Hergelegiu⁷²,
647 G. Herrera Corral¹¹, B.A. Hess³³, K.F. Hetland³⁵, B. Hippolyte⁵⁰, J. Hladky⁵⁵, P. Hristov³⁴, M. Huang¹⁷,
648 T.J. Humanic¹⁹, N. Hussain⁴¹, D. Hutter³⁹, D.S. Hwang²⁰, R. Ilkaev⁹³, I. Ilkiv⁷¹, M. Inaba¹²⁰,
649 G.M. Innocenti²⁵, C. Ionita³⁴, M. Ippolitov⁹⁴, M. Irfan¹⁸, M. Ivanov⁹¹, V. Ivanov⁷⁹, A. Jacholkowski²⁷,
650 P.M. Jacobs⁶⁸, C. Jahnke¹¹³, H.J. Jang⁶², M.A. Janik¹²⁶, P.H.S.Y. Jayarathna¹¹⁵, C. Jena²⁸, S. Jena¹¹⁵,

651 R.T. Jimenez Bustamante⁵⁸, P.G. Jones⁹⁶, H. Jung⁴⁰, A. Jusko⁹⁶, V. Kadyshevskiy⁶¹, S. Kalcher³⁹,
 652 P. Kalinak⁵⁴, A. Kalweit³⁴, J. Kamin⁴⁸, J.H. Kang¹³⁰, V. Kaplin⁷⁰, S. Kar¹²⁴, A. Karasu Uysal⁶³,
 653 O. Karavichev⁵¹, T. Karavicheva⁵¹, E. Karpechev⁵¹, U. Kebschull⁴⁷, R. Keidel¹³¹, D.L.D. Keijdener⁵²,
 654 M.M. Khan^{iii,18}, P. Khan⁹⁵, S.A. Khan¹²⁴, A. Khanzadeev⁷⁹, Y. Kharlov¹⁰⁶, B. Kileng³⁵, B. Kim¹³⁰,
 655 D.W. Kim^{62,40}, D.J. Kim¹¹⁶, J.S. Kim⁴⁰, M. Kim⁴⁰, M. Kim¹³⁰, S. Kim²⁰, T. Kim¹³⁰, S. Kirsch³⁹, I. Kisel³⁹,
 656 S. Kiselev⁵³, A. Kisiel¹²⁶, G. Kiss¹²⁸, J.L. Klay⁶, J. Klein⁸⁷, C. Klein-Bösing⁴⁹, A. Kluge³⁴, M.L. Knichel⁹¹,
 657 A.G. Knospe¹¹¹, C. Kobdaj^{34,108}, M. Kofarago³⁴, M.K. Köhler⁹¹, T. Kollegger³⁹, A. Kolojvari¹²³,
 658 V. Kondratiev¹²³, N. Kondratyeva⁷⁰, A. Konevskikh⁵¹, V. Kovalenko¹²³, M. Kowalski¹¹⁰, S. Kox⁶⁵,
 659 G. Koyithatta Meethalevedu⁴⁴, J. Kral¹¹⁶, I. Králik⁵⁴, F. Kramer⁴⁸, A. Kravčáková³⁸, M. Krelina³⁷,
 660 M. Kretz³⁹, M. Krivda^{96,54}, F. Krizek⁷⁷, E. Kryshen³⁴, M. Krzewicki⁹¹, V. Kučera⁷⁷, Y. Kucheriaev^{94,i},
 661 T. Kugathanan³⁴, C. Kuhn⁵⁰, P.G. Kuijjer⁷⁵, I. Kulakov⁴⁸, J. Kumar⁴⁴, P. Kurashvili⁷¹, A. Kurepin⁵¹,
 662 A.B. Kurepin⁵¹, A. Kuryakin⁹³, S. Kushpil⁷⁷, M.J. Kweon⁸⁷, Y. Kwon¹³⁰, P. Ladron de Guevara⁵⁸,
 663 C. Lagana Fernandes¹¹³, I. Lakomov⁴⁶, R. Langoy¹²⁵, C. Lara⁴⁷, A. Lardeux¹⁰⁷, A. Lattuca²⁵,
 664 S.L. La Pointe⁵², P. La Rocca²⁷, R. Lea²⁴, L. Leardini⁸⁷, G.R. Lee⁹⁶, I. Legrand³⁴, J. Lehnert⁴⁸,
 665 R.C. Lemmon⁷⁶, V. Lenti⁹⁸, E. Leogrande⁵², M. Leoncino²⁵, I. León Monzón¹¹², P. Lévai¹²⁸, S. Li^{64,7},
 666 J. Lien¹²⁵, R. Lietava⁹⁶, S. Lindal²¹, V. Lindenstruth³⁹, C. Lippmann⁹¹, M.A. Lisa¹⁹, H.M. Ljunggren³²,
 667 D.F. Lodato⁵², P.I. Loenne¹⁷, V.R. Loggins¹²⁷, V. Loginov⁷⁰, D. Lohner⁸⁷, C. Loizides⁶⁸, X. Lopez⁶⁴,
 668 E. López Torres⁹, X.-G. Lu⁸⁷, P. Luettig⁴⁸, M. Lunardon²⁸, G. Luparello⁵², C. Luzzi³⁴, R. Ma¹²⁹,
 669 A. Maevskaya⁵¹, M. Mager³⁴, D.P. Mahapatra⁵⁶, S.M. Mahmood²¹, A. Maire⁸⁷, R.D. Majka¹²⁹, M. Malaev⁷⁹,
 670 I. Maldonado Cervantes⁵⁸, L. Malinina^{iv,61}, D. Mal'Kevich⁵³, P. Malzacher⁹¹, A. Mamonov⁹³, L. Manceau¹⁰⁵,
 671 V. Manko⁹⁴, F. Manso⁶⁴, V. Manzari⁹⁸, M. Marchisone^{64,25}, J. Mareš⁵⁵, G.V. Margagliotti²⁴, A. Margotti⁹⁹,
 672 A. Marín⁹¹, C. Markert¹¹¹, M. Marquard⁴⁸, I. Martashvili¹¹⁸, N.A. Martin⁹¹, P. Martinengo³⁴, M.I. Martínez²,
 673 G. Martínez García¹⁰⁷, J. Martin Blanco¹⁰⁷, Y. Martynov³, A. Mas¹⁰⁷, S. Masciocchi⁹¹, M. Maserà²⁵,
 674 A. Masoni¹⁰⁰, L. Massacrier¹⁰⁷, A. Mastroserio³¹, A. Matyja¹¹⁰, C. Mayer¹¹⁰, J. Mazer¹¹⁸, M.A. Mazzoni¹⁰³,
 675 F. Meddi²², A. Menchaca-Rocha⁵⁹, J. Mercado Pérez⁸⁷, M. Meres³⁶, Y. Miake¹²⁰, K. Mikhaylov^{61,53},
 676 L. Milano³⁴, J. Milosevic^{v,21}, A. Mischke⁵², A.N. Mishra⁴⁵, D. Miśkowiec⁹¹, J. Mitra¹²⁴, C.M. Mitu⁵⁷,
 677 J. Mlynar¹²⁷, N. Mohammadi⁵², B. Mohanty^{73,124}, L. Molnar⁵⁰, L. Montaño Zetina¹¹, E. Montes¹⁰,
 678 M. Morando²⁸, D.A. Moreira De Godoy¹¹³, S. Moretto²⁸, A. Morsch³⁴, V. Muccifora⁶⁶, E. Mudnic¹⁰⁹,
 679 D. Mühlheim⁴⁹, S. Muhuri¹²⁴, M. Mukherjee¹²⁴, H. Müller³⁴, M.G. Munhoz¹¹³, S. Murray⁸³, L. Musa³⁴,
 680 J. Musinsky⁵⁴, B.K. Nandi⁴⁴, R. Nania⁹⁹, E. Nappi⁹⁸, C. Nattrass¹¹⁸, K. Nayak⁷³, T.K. Nayak¹²⁴,
 681 S. Nazarenko⁹³, A. Nedosekin⁵³, M. Nicassio⁹¹, M. Niculescu^{34,57}, B.S. Nielsen⁷⁴, S. Nikolaev⁹⁴,
 682 S. Nikulin⁹⁴, V. Nikulin⁷⁹, B.S. Nilsen⁸⁰, F. Noferini^{12,99}, P. Nomokonov⁶¹, G. Nooren⁵², J. Norman¹¹⁷,
 683 A. Nyanin⁹⁴, J. Nystrand¹⁷, H. Oeschler⁸⁷, S. Oh¹²⁹, S.K. Oh^{vi,40}, A. Okatan⁶³, L. Olah¹²⁸, J. Oleniac¹²⁶,
 684 A.C. Oliveira Da Silva¹¹³, J. Onderwaater⁹¹, C. Oppedisano¹⁰⁵, A. Ortiz Velasquez³², A. Oskarsson³²,
 685 J. Otwinowski⁹¹, K. Oyama⁸⁷, P. Sahoo⁴⁵, Y. Pachmayer⁸⁷, M. Pachr³⁷, P. Pagano²⁹, G. Paić⁵⁸, F. Painke³⁹,
 686 C. Pajares¹⁶, S.K. Pal¹²⁴, A. Palmeri¹⁰¹, D. Pant⁴⁴, V. Papikyan¹, G.S. Pappalardo¹⁰¹, P. Pareek⁴⁵,
 687 W.J. Park⁹¹, S. Parmar⁸¹, A. Passfeld⁴⁹, D.I. Patalakha¹⁰⁶, V. Paticchio⁹⁸, B. Paul⁹⁵, T. Pawlak¹²⁶,
 688 T. Peitzmann⁵², H. Pereira Da Costa¹⁴, E. Pereira De Oliveira Filho¹¹³, D. Peresunko⁹⁴, C.E. Pérez Lara⁷⁵,
 689 A. Pesci⁹⁹, V. Peskov⁴⁸, Y. Pestov⁵, V. Petráček³⁷, M. Petran³⁷, M. Petris⁷², M. Petrovici⁷², C. Petta²⁷,
 690 S. Piano¹⁰⁴, M. Pikna³⁶, P. Pillot¹⁰⁷, O. Pinazza^{99,34}, L. Pinsky¹¹⁵, D.B. Piyarathna¹¹⁵, M. Płoskoń⁶⁸,
 691 M. Planinic^{121,92}, J. Pluta¹²⁶, S. Pochybova¹²⁸, P.L.M. Podesta-Lerma¹¹², M.G. Poghosyan³⁴,
 692 E.H.O. Pohjoisaho⁴², B. Polichtchouk¹⁰⁶, N. Poljak⁹², A. Pop⁷², S. Porteboeuf-Houssais⁶⁴, J. Porter⁶⁸,
 693 B. Potukuchi⁸⁴, S.K. Prasad¹²⁷, R. Preghenella^{99,12}, F. Prino¹⁰⁵, C.A. Pruneau¹²⁷, I. Pshenichnov⁵¹,
 694 G. Puudu²³, P. Pujahari¹²⁷, V. Punin⁹³, J. Putschke¹²⁷, H. Qvigstad²¹, A. Rachevski¹⁰⁴, S. Raha⁴, J. Rak¹¹⁶,
 695 A. Rakotozafindrabe¹⁴, L. Ramello³⁰, R. Raniwala⁸⁵, S. Raniwala⁸⁵, S.S. Räsänen⁴², B.T. Rascanu⁴⁸,
 696 D. Rathee⁸¹, A.W. Rauf¹⁵, V. Razazi²³, K.F. Read¹¹⁸, J.S. Real⁶⁵, K. Redlich^{vii,71}, R.J. Reed¹²⁹,
 697 A. Rehman¹⁷, P. Reichelt⁴⁸, M. Reicher⁵², F. Reidt³⁴, R. Renfordt⁴⁸, A.R. Reolon⁶⁶, A. Reshetin⁵¹,
 698 F. Rettig³⁹, J.-P. Revol³⁴, K. Reygers⁸⁷, V. Riabov⁷⁹, R.A. Ricci⁶⁷, T. Richert³², M. Richter²¹, P. Riedler³⁴,
 699 W. Riegler³⁴, F. Riggi²⁷, A. Rivetti¹⁰⁵, E. Rocco⁵², M. Rodríguez Cahuantzi², A. Rodríguez Manso⁷⁵,
 700 K. Røed²¹, E. Rogochaya⁶¹, S. Rohni⁸⁴, D. Rohr³⁹, D. Röhrich¹⁷, R. Romita⁷⁶, F. Ronchetti⁶⁶,
 701 L. Ronflette¹⁰⁷, P. Rosnet⁶⁴, A. Rossi³⁴, F. Roukoutakis⁸², A. Roy⁴⁵, C. Roy⁵⁰, P. Roy⁹⁵,
 702 A.J. Rubio Montero¹⁰, R. Rui²⁴, R. Russo²⁵, E. Ryabinkin⁹⁴, Y. Ryabov⁷⁹, A. Rybicki¹¹⁰, S. Sadovsky¹⁰⁶,
 703 K. Šafařík³⁴, B. Sahlmüller⁴⁸, R. Sahoo⁴⁵, P.K. Sahu⁵⁶, J. Saini¹²⁴, S. Sakai⁶⁸, C.A. Salgado¹⁶, J. Salzwedel¹⁹,
 704 S. Sambyal⁸⁴, V. Samsonov⁷⁹, X. Sanchez Castro⁵⁰, F.J. Sánchez Rodríguez¹¹², L. Šándor⁵⁴, A. Sandoval⁵⁹,
 705 M. Sano¹²⁰, G. Santagati²⁷, D. Sarkar¹²⁴, E. Scapparone⁹⁹, F. Scarlassara²⁸, R.P. Scharenberg⁸⁹, C. Schiaua⁷²,
 706 R. Schicker⁸⁷, C. Schmidt⁹¹, H.R. Schmidt³³, S. Schuchmann⁴⁸, J. Schukraft³⁴, M. Schulc³⁷, T. Schuster¹²⁹,

707 Y. Schutz^{107,34}, K. Schwarz⁹¹, K. Schweda⁹¹, G. Scioli²⁶, E. Scomparin¹⁰⁵, R. Scott¹¹⁸, G. Segato²⁸,
708 J.E. Seger⁸⁰, Y. Sekiguchi¹¹⁹, I. Selyuzhenkov⁹¹, J. Seo⁹⁰, E. Serradilla^{10,59}, A. Sevcenco⁵⁷, A. Shabetai¹⁰⁷,
709 G. Shabratova⁶¹, R. Shahoyan³⁴, A. Shangaraev¹⁰⁶, N. Sharma¹¹⁸, S. Sharma⁸⁴, K. Shigaki⁴³, K. Shtejer²⁵,
710 Y. Sibiriyak⁹⁴, S. Siddhanta¹⁰⁰, T. Siemiarczuk⁷¹, D. Silvermyr⁷⁸, C. Silvestre⁶⁵, G. Simatovic¹²¹,
711 R. Singaraju¹²⁴, R. Singh⁸⁴, S. Singha^{124,73}, V. Singhal¹²⁴, B.C. Sinha¹²⁴, T. Sinha⁹⁵, B. Sitar³⁶, M. Sitta³⁰,
712 T.B. Skaali²¹, K. Skjerdal¹⁷, M. Slupecki¹¹⁶, N. Smirnov¹²⁹, R.J.M. Snellings⁵², C. Sogaard³², R. Soltz⁶⁹,
713 J. Song⁹⁰, M. Song¹³⁰, F. Soramel²⁸, S. Sorensen¹¹⁸, M. Spacek³⁷, E. Spiriti⁶⁶, I. Sputowska¹¹⁰,
714 M. Spyropoulou-Stassinaki⁸², B.K. Srivastava⁸⁹, J. Stachel⁸⁷, I. Stan⁵⁷, G. Stefanek⁷¹, M. Steinpreis¹⁹,
715 E. Stenlund³², G. Steyn⁶⁰, J.H. Stiller⁸⁷, D. Stocco¹⁰⁷, M. Stolpovskiy¹⁰⁶, P. Strmen³⁶, A.A.P. Suaide¹¹³,
716 T. Sugitate⁴³, C. Suire⁴⁶, M. Suleymanov¹⁵, R. Sultanov⁵³, M. Šumbera⁷⁷, T. Susa⁹², T.J.M. Symons⁶⁸,
717 A. Szabo³⁶, A. Szanto de Toledo¹¹³, I. Szarka³⁶, A. Szczepankiewicz³⁴, M. Szymanski¹²⁶, J. Takahashi¹¹⁴,
718 M.A. Tangaro³¹, J.D. Tapia Takaki^{viii,46}, A. Tarantola Peloni⁴⁸, A. Tarazona Martinez³⁴, M.G. Tarzila⁷²,
719 A. Tauro³⁴, G. Tejeda Muñoz², A. Telesca³⁴, C. Terrevoli²³, J. Thäder⁹¹, D. Thomas⁵², R. Tieulent¹²²,
720 A.R. Timmins¹¹⁵, A. Toia¹⁰², V. Trubnikov³, W.H. Trzaska¹¹⁶, T. Tsuji¹¹⁹, A. Tumkin⁹³, R. Turrisi¹⁰²,
721 T.S. Tveter²¹, K. Ullaland¹⁷, A. Uras¹²², G.L. Usai²³, M. Vajzer⁷⁷, M. Vala^{54,61}, L. Valencia Palomo⁶⁴,
722 S. Vallero⁸⁷, P. Vande Vyvre³⁴, J. Van Der Maarel⁵², J.W. Van Hoorne³⁴, M. van Leeuwen⁵², A. Vargas²,
723 M. Vargyas¹¹⁶, R. Varma⁴⁴, M. Vasileiou⁸², A. Vasiliev⁹⁴, V. Vechernin¹²³, M. Veldhoen⁵², A. Velure¹⁷,
724 M. Venaruzzo^{24,67}, E. Vercellin²⁵, S. Vergara Limón², R. Vernet⁸, M. Verweij¹²⁷, L. Vickovic¹⁰⁹, G. Viesti²⁸,
725 J. Viinikainen¹¹⁶, Z. Vilakazi⁶⁰, O. Villalobos Baillie⁹⁶, A. Vinogradov⁹⁴, L. Vinogradov¹²³, Y. Vinogradov⁹³,
726 T. Virgili²⁹, Y.P. Viyogi¹²⁴, A. Vodopyanov⁶¹, M.A. Völkl⁸⁷, K. Voloshin⁵³, S.A. Voloshin¹²⁷, G. Volpe³⁴,
727 B. von Haller³⁴, I. Vorobyev¹²³, D. Vranic^{34,91}, J. Vrláková³⁸, B. Vulpescu⁶⁴, A. Vyushin⁹³, B. Wagner¹⁷,
728 J. Wagner⁹¹, V. Wagner³⁷, M. Wang^{7,107}, Y. Wang⁸⁷, D. Watanabe¹²⁰, M. Weber¹¹⁵, J.P. Wessels⁴⁹,
729 U. Westerhoff⁴⁹, J. Wiechula³³, J. Wikne²¹, M. Wilde⁴⁹, G. Wilk⁷¹, J. Wilkinson⁸⁷, M.C.S. Williams⁹⁹,
730 B. Windelband⁸⁷, M. Winn⁸⁷, C.G. Yaldo¹²⁷, Y. Yamaguchi¹¹⁹, H. Yang⁵², P. Yang⁷, S. Yang¹⁷, S. Yano⁴³,
731 S. Yasnopolskiy⁹⁴, J. Yi⁹⁰, Z. Yin⁷, I.-K. Yoo⁹⁰, I. Yushmanov⁹⁴, V. Zaccolo⁷⁴, C. Zach³⁷, A. Zaman¹⁵,
732 C. Zampolli⁹⁹, S. Zaporozhets⁶¹, A. Zarochentsev¹²³, P. Závada⁵⁵, N. Zaviyalov⁹³, H. Zbroszczyk¹²⁶,
733 I.S. Zgura⁵⁷, M. Zhalov⁷⁹, H. Zhang⁷, X. Zhang^{7,68}, Y. Zhang⁷, C. Zhao²¹, N. Zhigareva⁵³, D. Zhou⁷,
734 F. Zhou⁷, Y. Zhou⁵², Zhou, Zhuo¹⁷, H. Zhu⁷, J. Zhu⁷, X. Zhu⁷, A. Zichichi^{12,26}, A. Zimmermann⁸⁷,
735 M.B. Zimmermann^{49,34}, G. Zinovjev³, Y. Zoccarato¹²², M. Zyzak⁴⁸

Affiliation notes

- 736 ⁱ Deceased
737 ⁱⁱ Also at: St. Petersburg State Polytechnical University
738 ⁱⁱⁱ Also at: Department of Applied Physics, Aligarh Muslim University, Aligarh, India
739 ^{iv} Also at: M.V. Lomonosov Moscow State University, D.V. Skobeltsyn Institute of Nuclear Physics,
740 Moscow, Russia
741 ^v Also at: University of Belgrade, Faculty of Physics and "Vinča" Institute of Nuclear Sciences, Belgrade,
742 Serbia
743 ^{vi} Permanent Address: Permanent Address: Konkuk University, Seoul, Korea
744 ^{vii} Also at: Institute of Theoretical Physics, University of Wrocław, Wrocław, Poland
745 ^{viii} Also at: University of Kansas, Lawrence, KS, United States
746

Collaboration Institutes

- 747 ¹ A.I. Alikhanyan National Science Laboratory (Yerevan Physics Institute) Foundation, Yerevan, Armenia
748 ² Benemérita Universidad Autónoma de Puebla, Puebla, Mexico
749 ³ Bogolyubov Institute for Theoretical Physics, Kiev, Ukraine
750 ⁴ Bose Institute, Department of Physics and Centre for Astroparticle Physics and Space Science (CAPSS),
751 Kolkata, India
752 ⁵ Budker Institute for Nuclear Physics, Novosibirsk, Russia
753 ⁶ California Polytechnic State University, San Luis Obispo, CA, United States
754 ⁷ Central China Normal University, Wuhan, China
755 ⁸ Centre de Calcul de l'IN2P3, Villeurbanne, France
756 ⁹ Centro de Aplicaciones Tecnológicas y Desarrollo Nuclear (CEADEN), Havana, Cuba
757 ¹⁰ Centro de Investigaciones Energéticas Medioambientales y Tecnológicas (CIEMAT), Madrid, Spain
758 ¹¹ Centro de Investigación y de Estudios Avanzados (CINVESTAV), Mexico City and Mérida, Mexico
759

- 760 12 Centro Fermi - Museo Storico della Fisica e Centro Studi e Ricerche “Enrico Fermi”, Rome, Italy
761 13 Chicago State University, Chicago, USA
762 14 Commissariat à l’Energie Atomique, IRFU, Saclay, France
763 15 COMSATS Institute of Information Technology (CIIT), Islamabad, Pakistan
764 16 Departamento de Física de Partículas and IGFAE, Universidad de Santiago de Compostela, Santiago de
765 Compostela, Spain
766 17 Department of Physics and Technology, University of Bergen, Bergen, Norway
767 18 Department of Physics, Aligarh Muslim University, Aligarh, India
768 19 Department of Physics, Ohio State University, Columbus, OH, United States
769 20 Department of Physics, Sejong University, Seoul, South Korea
770 21 Department of Physics, University of Oslo, Oslo, Norway
771 22 Dipartimento di Fisica dell’Università ‘La Sapienza’ and Sezione INFN Rome, Italy
772 23 Dipartimento di Fisica dell’Università and Sezione INFN, Cagliari, Italy
773 24 Dipartimento di Fisica dell’Università and Sezione INFN, Trieste, Italy
774 25 Dipartimento di Fisica dell’Università and Sezione INFN, Turin, Italy
775 26 Dipartimento di Fisica e Astronomia dell’Università and Sezione INFN, Bologna, Italy
776 27 Dipartimento di Fisica e Astronomia dell’Università and Sezione INFN, Catania, Italy
777 28 Dipartimento di Fisica e Astronomia dell’Università and Sezione INFN, Padova, Italy
778 29 Dipartimento di Fisica ‘E.R. Caianiello’ dell’Università and Gruppo Collegato INFN, Salerno, Italy
779 30 Dipartimento di Scienze e Innovazione Tecnologica dell’Università del Piemonte Orientale and Gruppo
780 Collegato INFN, Alessandria, Italy
781 31 Dipartimento Interateneo di Fisica ‘M. Merlin’ and Sezione INFN, Bari, Italy
782 32 Division of Experimental High Energy Physics, University of Lund, Lund, Sweden
783 33 Eberhard Karls Universität Tübingen, Tübingen, Germany
784 34 European Organization for Nuclear Research (CERN), Geneva, Switzerland
785 35 Faculty of Engineering, Bergen University College, Bergen, Norway
786 36 Faculty of Mathematics, Physics and Informatics, Comenius University, Bratislava, Slovakia
787 37 Faculty of Nuclear Sciences and Physical Engineering, Czech Technical University in Prague, Prague,
788 Czech Republic
789 38 Faculty of Science, P.J. Šafárik University, Košice, Slovakia
790 39 Frankfurt Institute for Advanced Studies, Johann Wolfgang Goethe-Universität Frankfurt, Frankfurt,
791 Germany
792 40 Gangneung-Wonju National University, Gangneung, South Korea
793 41 Gauhati University, Department of Physics, Guwahati, India
794 42 Helsinki Institute of Physics (HIP), Helsinki, Finland
795 43 Hiroshima University, Hiroshima, Japan
796 44 Indian Institute of Technology Bombay (IIT), Mumbai, India
797 45 Indian Institute of Technology Indore, Indore (IITI), India
798 46 Institut de Physique Nucléaire d’Orsay (IPNO), Université Paris-Sud, CNRS-IN2P3, Orsay, France
799 47 Institut für Informatik, Johann Wolfgang Goethe-Universität Frankfurt, Frankfurt, Germany
800 48 Institut für Kernphysik, Johann Wolfgang Goethe-Universität Frankfurt, Frankfurt, Germany
801 49 Institut für Kernphysik, Westfälische Wilhelms-Universität Münster, Münster, Germany
802 50 Institut Pluridisciplinaire Hubert Curien (IPHC), Université de Strasbourg, CNRS-IN2P3, Strasbourg,
803 France
804 51 Institute for Nuclear Research, Academy of Sciences, Moscow, Russia
805 52 Institute for Subatomic Physics of Utrecht University, Utrecht, Netherlands
806 53 Institute for Theoretical and Experimental Physics, Moscow, Russia
807 54 Institute of Experimental Physics, Slovak Academy of Sciences, Košice, Slovakia
808 55 Institute of Physics, Academy of Sciences of the Czech Republic, Prague, Czech Republic
809 56 Institute of Physics, Bhubaneswar, India
810 57 Institute of Space Science (ISS), Bucharest, Romania
811 58 Instituto de Ciencias Nucleares, Universidad Nacional Autónoma de México, Mexico City, Mexico
812 59 Instituto de Física, Universidad Nacional Autónoma de México, Mexico City, Mexico
813 60 iThemba LABS, National Research Foundation, Somerset West, South Africa
814 61 Joint Institute for Nuclear Research (JINR), Dubna, Russia
815 62 Korea Institute of Science and Technology Information, Daejeon, South Korea

- 816 63 KTO Karatay University, Konya, Turkey
817 64 Laboratoire de Physique Corpusculaire (LPC), Clermont Université, Université Blaise Pascal,
818 CNRS-IN2P3, Clermont-Ferrand, France
819 65 Laboratoire de Physique Subatomique et de Cosmologie, Université Grenoble-Alpes, CNRS-IN2P3,
820 Grenoble, France
821 66 Laboratori Nazionali di Frascati, INFN, Frascati, Italy
822 67 Laboratori Nazionali di Legnaro, INFN, Legnaro, Italy
823 68 Lawrence Berkeley National Laboratory, Berkeley, CA, United States
824 69 Lawrence Livermore National Laboratory, Livermore, CA, United States
825 70 Moscow Engineering Physics Institute, Moscow, Russia
826 71 National Centre for Nuclear Studies, Warsaw, Poland
827 72 National Institute for Physics and Nuclear Engineering, Bucharest, Romania
828 73 National Institute of Science Education and Research, Bhubaneswar, India
829 74 Niels Bohr Institute, University of Copenhagen, Copenhagen, Denmark
830 75 Nikhef, National Institute for Subatomic Physics, Amsterdam, Netherlands
831 76 Nuclear Physics Group, STFC Daresbury Laboratory, Daresbury, United Kingdom
832 77 Nuclear Physics Institute, Academy of Sciences of the Czech Republic, Řež u Prahy, Czech Republic
833 78 Oak Ridge National Laboratory, Oak Ridge, TN, United States
834 79 Petersburg Nuclear Physics Institute, Gatchina, Russia
835 80 Physics Department, Creighton University, Omaha, NE, United States
836 81 Physics Department, Panjab University, Chandigarh, India
837 82 Physics Department, University of Athens, Athens, Greece
838 83 Physics Department, University of Cape Town, Cape Town, South Africa
839 84 Physics Department, University of Jammu, Jammu, India
840 85 Physics Department, University of Rajasthan, Jaipur, India
841 86 Physik Department, Technische Universität München, Munich, Germany
842 87 Physikalisches Institut, Ruprecht-Karls-Universität Heidelberg, Heidelberg, Germany
843 88 Politecnico di Torino, Turin, Italy
844 89 Purdue University, West Lafayette, IN, United States
845 90 Pusan National University, Pusan, South Korea
846 91 Research Division and ExtreMe Matter Institute EMMI, GSI Helmholtzzentrum für
847 Schwerionenforschung, Darmstadt, Germany
848 92 Rudjer Bošković Institute, Zagreb, Croatia
849 93 Russian Federal Nuclear Center (VNIIEF), Sarov, Russia
850 94 Russian Research Centre Kurchatov Institute, Moscow, Russia
851 95 Saha Institute of Nuclear Physics, Kolkata, India
852 96 School of Physics and Astronomy, University of Birmingham, Birmingham, United Kingdom
853 97 Sección Física, Departamento de Ciencias, Pontificia Universidad Católica del Perú, Lima, Peru
854 98 Sezione INFN, Bari, Italy
855 99 Sezione INFN, Bologna, Italy
856 100 Sezione INFN, Cagliari, Italy
857 101 Sezione INFN, Catania, Italy
858 102 Sezione INFN, Padova, Italy
859 103 Sezione INFN, Rome, Italy
860 104 Sezione INFN, Trieste, Italy
861 105 Sezione INFN, Turin, Italy
862 106 SSC IHEP of NRC Kurchatov institute, Protvino, Russia
863 107 SUBATECH, Ecole des Mines de Nantes, Université de Nantes, CNRS-IN2P3, Nantes, France
864 108 Suranaree University of Technology, Nakhon Ratchasima, Thailand
865 109 Technical University of Split FESB, Split, Croatia
866 110 The Henryk Niewodniczanski Institute of Nuclear Physics, Polish Academy of Sciences, Cracow, Poland
867 111 The University of Texas at Austin, Physics Department, Austin, TX, USA
868 112 Universidad Autónoma de Sinaloa, Culiacán, Mexico
869 113 Universidade de São Paulo (USP), São Paulo, Brazil
870 114 Universidade Estadual de Campinas (UNICAMP), Campinas, Brazil
871 115 University of Houston, Houston, TX, United States

- 872 116 University of Jyväskylä, Jyväskylä, Finland
873 117 University of Liverpool, Liverpool, United Kingdom
874 118 University of Tennessee, Knoxville, TN, United States
875 119 University of Tokyo, Tokyo, Japan
876 120 University of Tsukuba, Tsukuba, Japan
877 121 University of Zagreb, Zagreb, Croatia
878 122 Université de Lyon, Université Lyon 1, CNRS/IN2P3, IPN-Lyon, Villeurbanne, France
879 123 V. Fock Institute for Physics, St. Petersburg State University, St. Petersburg, Russia
880 124 Variable Energy Cyclotron Centre, Kolkata, India
881 125 Vestfold University College, Tonsberg, Norway
882 126 Warsaw University of Technology, Warsaw, Poland
883 127 Wayne State University, Detroit, MI, United States
884 128 Wigner Research Centre for Physics, Hungarian Academy of Sciences, Budapest, Hungary
885 129 Yale University, New Haven, CT, United States
886 130 Yonsei University, Seoul, South Korea
887 131 Zentrum für Technologietransfer und Telekommunikation (ZTT), Fachhochschule Worms, Worms,
888 Germany